

## Chapter 3

# Conceptual Design of Long-Stroke Planar Actuator

This chapter presents the fundamental conceptual design of a long-stroke 3-DOF planar actuator.

## 3. Conceptual Design of Long-Stroke Planar Actuator

This chapter proposes a novel synchronous planar actuator using spatially superimposed magnetic circuits for the 2-D motion controls of a mover, enabling comprehensive drive over a wide movable area on a plane by means of a few armature conductors.

### 3.1. Conceptual Design

In this study, I present the design for a novel synchronous planar actuator with a permanent-magnet mover capable of long-stroke high-performance planar motions achieved using just a few armature conductors. This section introduces the design considerations, basic drive principle of linear synchronous motors, and a method of extending linear motion to planar motion.

#### 3.1.1. Design Considerations

As mentioned in Chapter 2, synchronous planar actuators with a permanent-magnet mover generally have good controllability of their driving forces. However, this type of planar actuator often has a significant problem in that the movable area is quite narrow. This problem is caused by spatially separating multiple pairs of permanent-magnet arrays and armature conductors for the 2-D drives, so as to make it easy to independently control the MDOF motions. To eliminate this problem, I propose a novel synchronous planar actuator using spatially superimposed magnetic circuits for the 2-D drives achieved by the use of a 2-D permanent-magnet array and overlapped armature conductors. My proposed planar actuator has the following features:

- the advantage of long-stroke planar motions achieved using only a few conductors; but
- the disadvantage of difficulty in realizing independent control due to the spatial superimposition of the magnetic circuits for each directional drive.

Therefore, in this study, design of the electromechanical system of the planar actuator is the most important issue so that the mover motions in each direction can be decoupled by spatially superimposed magnetic circuits.

### 3.1.2. Basic Coreless Linear Synchronous Motor with Moving Magnets

This subsection introduces the drive principle of a coreless linear synchronous motor with a permanent-magnet mover, on which my proposed planar actuator is based. Figure 3.1.2-1 shows a schematic view of a coreless linear synchronous motor consisting of three-phase armature conductors and a multipole permanent-magnet array. The magnet array generates a sinusoidally distributed flux density  $B_z$  on the surface of the stationary armature conductors along the  $x$ -direction, the pole-pitch length of which is  $\tau_0$  as shown in the following equation:

$$B_z(x) = B_{z0} \cos\left(\frac{\pi}{\tau_0}(x - x_0)\right) \dots\dots\dots(3.1.2-1)$$

where  $B_{z0}$  and  $x_0$  are an amplitude of the flux density and the position of the magnet array, respectively. The following three-phase currents  $i_u$ ,  $i_v$ , and  $i_w$  are supplied to the three-phase armature conductors as shown in Fig. 3.1.2-2:

$$i_u = I_0 \sin(\theta_s) \dots\dots\dots(3.1.2-2)$$

$$i_v = I_0 \sin\left(\theta_s + \frac{2\pi}{3}\right) \dots\dots\dots(3.1.2-3)$$

$$i_w = I_0 \sin\left(\theta_s + \frac{4\pi}{3}\right) \dots\dots\dots(3.1.2-4)$$

where  $I_0$  and  $\theta_s$  are an amplitude and phase of the three-phase currents, respectively. Electromagnetic force acting on each armature conductor can be calculated from a Lorentz force equation,  $F_L = i \times B$ , and the reaction forces  $F_x$  of all the armature conductors act on the mover as follows:

$$\begin{aligned} F_x &= i_u B_z(0) - i_v B_z\left(\frac{\tau_0}{3}\right) + i_w B_z\left(\frac{2\tau_0}{3}\right) - i_u B_z(\tau_0) + i_v B_z\left(\frac{4\tau_0}{3}\right) - i_w B_z\left(\frac{5\tau_0}{3}\right) \\ &= \sum_{n=0}^5 I_0 \sin\left(\theta_s - \frac{n\pi}{3}\right) \cdot B_{z0} \cos\left(\frac{n\pi}{3} - \frac{\pi}{\tau_0} x_0\right) \dots\dots\dots(3.1.2-5) \\ &= 3B_{z0} I_0 \sin\left(\theta_s - \frac{\pi}{\tau_0} x_0\right) \end{aligned}$$

Equation (3.2.1-5) indicates that the driving forces are proportional and sinusoidal to the amplitude and phase of the three-phase currents, respectively.

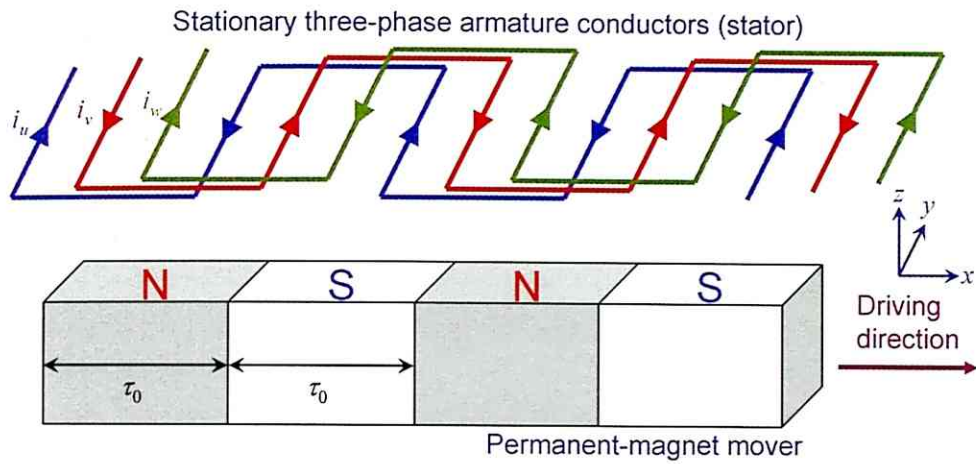


Fig. 3.1.2-1: Schematic view of a basic coreless linear synchronous motor with a permanent-magnet mover.

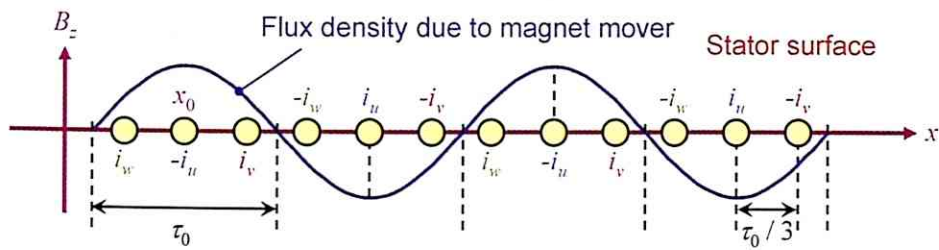


Fig. 3.1.2-2: Supplied armature currents and flux density due to the magnet mover on the stator surface.

### 3.1.3. Extension of Linear Motion to Planar Motion

To generate driving forces in the  $x$ - and  $y$ -directions using spatially superimposed magnetic circuits, there are two requirements:

- a permanent-magnet mover generating superimposed magnetic fields for the  $x$ - and  $y$ -directional drives is required.
- armature currents along two or more directions are required to be supplied to the region where the magnetic fields act.

This study deals with a 2-D Halbach permanent-magnet mover as shown in Eq. (2.3.4-2) in order to generate the superimposed magnetic fields with high intensity and quasi-sinusoidal distribution in the  $x$ - and  $y$ -directions. The magnet mover is tilted by 45 deg as shown in Fig. 2.3.4-11. Overlapped armature conductors for the  $x$ - and  $y$ -directional drives are utilized in order to always act the magnetic fields, regardless of the mover positions.

With this in mind, the planar actuator was conceptually designed and manufactured as shown in Figs. 3.1.3-1 and 3.1.3-2. The fundamental structure, drive principle, and decoupled motion-control system are introduced in the following sections.

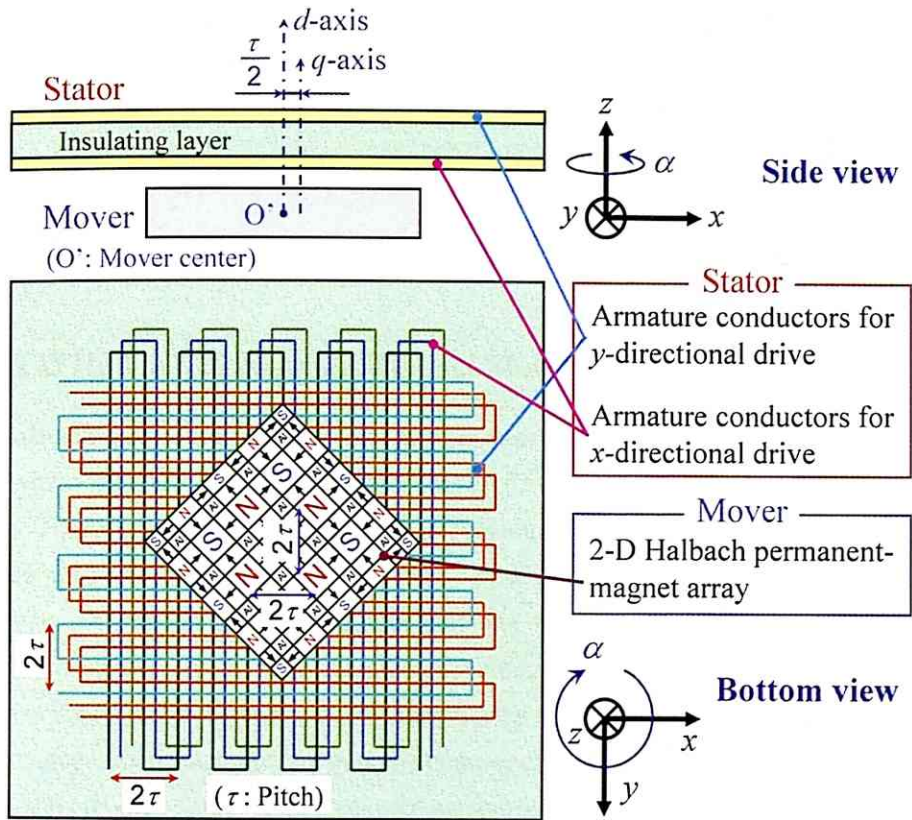
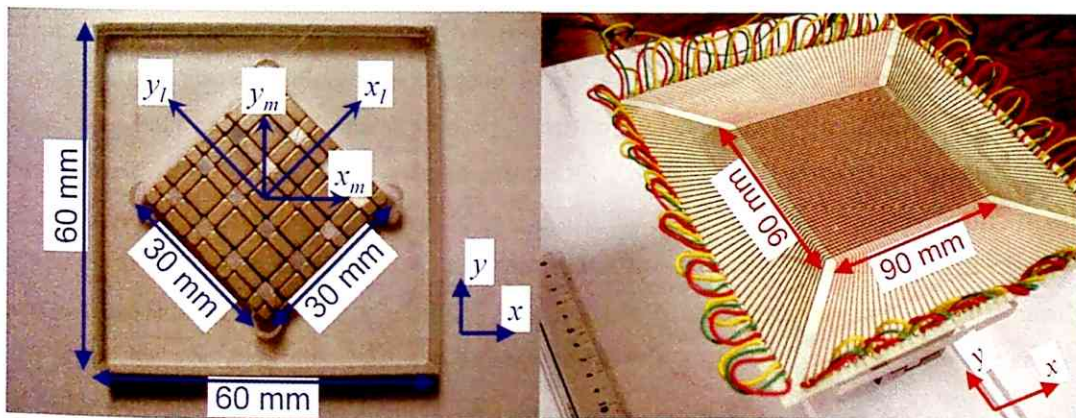


Fig. 3.1.3-1: Fundamental structure of planar actuator dealt with in this study.



(a) Top view of mover.

(b) Perspective view of stator.

Fig. 3.1.3-2: Mover and stator structures of planar actuator.

## 3.2. Fundamental Structure

Figure 3.1.3-1 shows the fundamental structure of the planar actuator dealt with in this study. The planar actuator has a mover consisting of a 2-D Halbach permanent-magnet array and six stationary overlapped armature conductors, which are arranged in two layers of three. This section introduces the fundamental structure of the planar actuator.

### 3.2.1. 2-D Halbach Permanent-Magnet Mover

A Halbach permanent-magnet array generates a high-intensity magnetic field with a quasi-sinusoidal distribution along the array direction on one side of the magnet array [Hal86]. Therefore, applying Halbach permanent-magnet arrays to coreless electric machines both enhances their driving forces and diminishes their force ripples [How01]. The mover, with which this study deals, consists of five-pole-and-nine-segment Halbach permanent-magnet arrays arranged two-dimensionally in the  $x_l$ - and  $y_l$ -directions as shown in Fig. 3.2.1-1. Table 3.2.1-1 shows the specifications of the 2-D permanent-magnet mover. Each permanent-magnet component was designed so as to maximize the ratio of the driving force of the planar actuator to the total mass of the mover at a nominal gap between the mover and stator, which is 0.5 mm [Ohs03]. Dr. Ken Ohashi and Mr. Yasuaki Aoyama, Shin-Etsu Chemical Co., Ltd., kindly fabricated the 2-D Halbach permanent-magnet array by bonding each permanent magnet onto a 1-mm-thick iron plate with DYMAX 848 (Sumitomo 3M Limited), which is an ultraviolet cure adhesive, and thus provided the magnet array for this study. The flux density of their fabricated magnet array was tested by scanning with a Hall element installed on a 10- $\mu$ m-resolution three-axis robot manipulator (NSK Ltd.), which consists of three stepping motors with a rack-and-pinion. Figure 3.2.1-2 shows the measurement result of the  $z$ -directional flux density  $B_z$  on a plane 0.5 mm above the surface of the magnet array. Figure 3.2.1-2 indicates that the flux density  $B_z$  is distributed quasi-sinusoidally in the  $x_l$ - and  $y_l$ -directions, and can be approximately expressed near the mover center as follows:

$$B_z(x_l, y_l, z) = B_{zm}(z) \cos\left(\frac{\pi}{\tau_{PM}} x_l\right) \cos\left(\frac{\pi}{\tau_{PM}} y_l\right) \dots\dots\dots (3.2.1-1)$$

where  $B_{zm}$  is a maximum flux density on a plane distant from the mover surface in the  $z$ -direction, and  $\tau_{PM}$  is pole-pitch length in the  $x_l$ - and  $y_l$ -directions. Equation (3.2.1-1) can

be rewritten by utilizing the  $x_m$ - $y_m$  coordinate, fixed with the mover, as follows:

$$B_z(x_m, y_m, z) = \frac{B_{zm}(z)}{2} \left( \cos\left(\frac{\pi}{\tau} x_m\right) + \cos\left(\frac{\pi}{\tau} y_m\right) \right) \dots\dots\dots (3.2.1-2)$$

Equation (3.2.1-2) indicates that the permanent-magnet mover generates multipole magnetic fields superimposed spatially with the same lengths of pole pitch  $\tau$  in the  $x_m$ - and  $y_m$ -directions. Pole pitch  $\tau$  in the  $x_m$ - and  $y_m$ -directions can be expressed by the pole pitch  $\tau_{PM}$  in the  $x_l$ - and  $y_l$ -directions as follows:

$$\tau = \frac{\tau_{PM}}{\sqrt{2}} \dots\dots\dots (3.2.1-3)$$

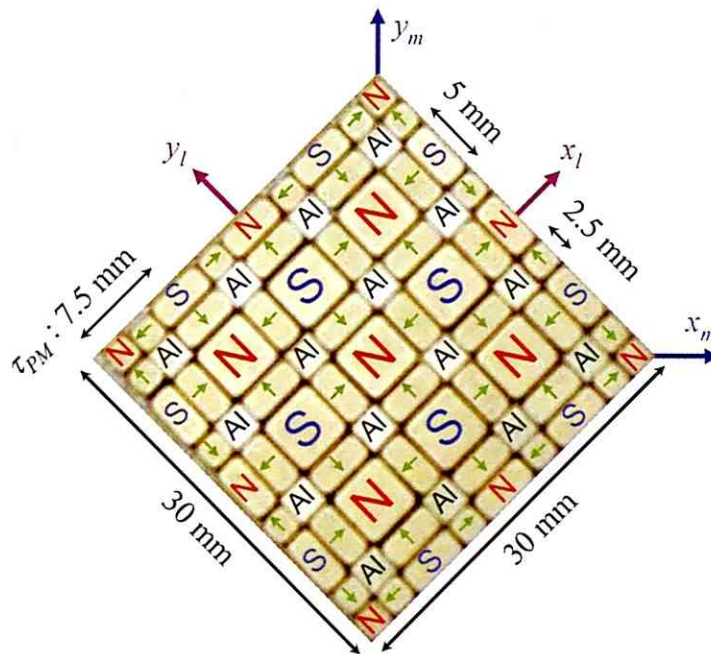


Fig. 3.2.1-1: Dimension and magnetization of permanent-magnet mover.

Table 3.2.1-1: Specifications of 2-D permanent-magnet mover.

Material	NdFeB (Shin-Etsu Chemical Co., Ltd.)
Residual flux density $B_r$	1.25 – 1.30 T
Overall dimension	30 mm × 30 mm × 6 mm
PM component	5 mm × 5 mm × 5 mm, or 5 mm × 5 mm × 2.5 mm
Dimension of back iron	30 mm × 30 mm × 1 mm
Total mass	37.3 g

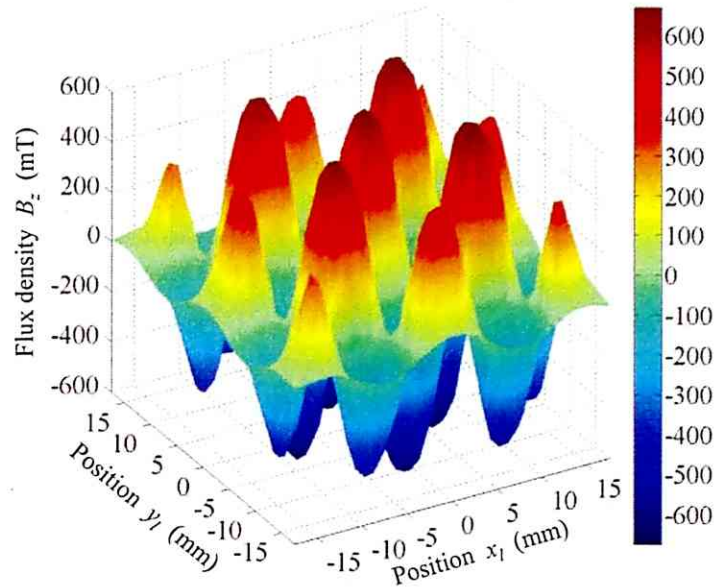


Fig. 3.2.1-2: Flux density distribution  $B_z$  generated by the permanent-magnet mover on the plane 0.5 mm above the surface of the mover.

### 3.2.2. Stationary Overlapped Armature Conductors

There are two sets of three stationary armature conductors arranged on two layers on a double-layered printed circuit board, for the  $x$ - and  $y$ -directional drives. All the armature conductors are meander-shaped and are designed so that pitch length of the meander shape is  $\tau$ , corresponding to the pole-pitch length of the permanent-magnet mover in the  $x_m$ - and  $y_m$ -directions. The three armature conductors arranged on each layer are mutually distant at  $2\tau / 3$  intervals, and supply the three-phase alternating currents for the  $x$ - or  $y$ -directional drives. Between the two layers, there is a thin insulating layer that creates different gap lengths: the gap length between the mover and the armature conductors for the  $x$ - directional drive is different from that between the mover and the armature conductors for the  $y$ -directional drive. So, it is extremely important to make the insulating layer as thin as possible.

All the armature conductors are arranged over the stator, and so are always subjected to the magnetic field for the  $x$ - and  $y$ -directional drives generated by the permanent-magnet mover regardless of the mover position on the stator. Therefore, the mover can travel over the wide stator area. Furthermore, lengthening all the armature conductors extends the movable area without increasing the number of armature

conductors, thus the power-supply system does not become complicated. Table 3.2.2-1 shows the specifications of the double-layered printed circuit board hosting the armature conductors.

Table 3.2.2-1: Specifications of double-layered printed circuit board.

Number of conductor layers	2
Pitch of meander pattern, $\tau$	5.3 mm
Number of turns of meander pattern	15
Width of conductors	0.8 mm
Thickness of conductors	35 $\mu\text{m}$
Thickness of insulating layer	0.1 mm
Resistance of each conductor	1.6 $\Omega$
Inductance of each conductor	3.8 $\mu\text{H}$

### 3.2.3. Drive Principle

When the  $y_m$ - and  $x_m$ -axes, fixed with the mover, are parallel to the armature conductors for the  $x$ - and  $y$ -directional drives as shown in Fig. 3.1.3-1, the mover generates a quasi-sinusoidal flux-density distribution with pole pitch  $\tau$ , corresponding to the meander-shaped pitch in length, in the  $x$ - and  $y$ -directions as shown in Eq. (3.2.1-2). Therefore, supplying two sources of three-phase alternating current to the two sets of three armature conductors forms two magnetic circuits, as in linear synchronous motors, in the  $x$ - and  $y$ -directions, and consequently generates driving forces in the  $x$ - and  $y$ -directions. Although not all the magnetic circuits formed over the stator are mutually-separated, exciting the armature conductors for the  $x$ - and  $y$ -directional drives independently generates driving forces in the  $x$ - and  $y$ -directions, respectively, because of their mutually-orthogonal directions.

Displacing the  $\alpha$ -position (yaw position) and expressing the rotational position around the  $z$ -axis, not only influences the translational forces, it but also generates torque around the  $z$ -axis because of the broken symmetry of the spatial distribution of the translational forces acting on the mover. So it is extremely important to simultaneously control not only the  $x$ - and  $y$ -motions, but also the  $\alpha$ -motions. Therefore, the characteristics of the translational forces and torque for the  $\alpha$ -positions need to be investigated in detail.

### 3.3. Static Force Characteristics

Investigation of 3-DOF ( $x$ ,  $y$ , and  $\alpha$ ) driving force characteristics is essential in controlling 3-DOF motion. This section presents a numerically analytical investigation of the static driving forces with 3 DOF. First, the analytical model and calculation method of the driving forces are introduced, and then the analysis results are described.

#### 3.3.1. Analytical Model

The driving forces acting on the mover of the planar actuator can be calculated from armature current  $i$  and flux density  $B$  using the Lorentz force equation  $F_L = i \times B$ . Figure 3.3.1-1 shows the configuration of the mover and stator of the analysis model, and shows that the mover is displaced in the  $\alpha$ -direction and an armature current  $i_{jk}$  is supplied to an armature conductor  $l_{jk}$  ( $j = x$  or  $y$ ,  $k = u, v$ , or  $w$ ), where  $j$  ( $= x$  or  $y$ ) and  $k$  ( $= u, v$ , or  $w$ ) express the driving direction and phase name of the three-phase currents, respectively. When a line element  $dl_{jk}$ , which is a small part of the armature conductor  $l_{jk}$  is in the flux density  $B$ , translational force  $dF$  and torque  $dT$  acting on the line element  $dl_{jk}$  can be expressed as follows:

$$dF = (i_{jk} \times B) dl_{jk} \dots\dots\dots(3.3.1-1)$$

$$dT = (r_{jk} - r_m) \times (i_{jk} \times B) dl_{jk} \dots\dots\dots(3.3.1-2)$$

where  $r_{jk}$  and  $r_m$  are position vectors of the line element  $dl_{jk}$  and the mover center O' with respect to the stationary coordinate  $x_s, y_s, z_s$ . Next, integration of  $dF$  and  $dT$  over all the armature conductors gives the total translational force and torque acting on the mover as follows:

$$F = -\sum_{j,k} \int_{jk} dF = -\sum_{j,k} \int_{jk} (i_{jk} \times B) dl_{jk} \dots\dots\dots(3.3.1-3)$$

$$T = -\sum_{j,k} \int_{jk} dT = -\sum_{j,k} \int_{jk} (r_{jk} - r_m) \times (i_{jk} \times B) dl_{jk} \dots\dots\dots(3.3.1-4)$$

From these equations, if the armature currents  $i_{jk}$  and flux density  $B$  are constant, the translational forces  $F$  and torques  $T$  are proportional to the square and cube of the mover, respectively, because the lengths of the integration passes in Eq. (3.3.1-3) and (3.3.1-4) are proportional to the square of the mover. On the other hand, if mass density  $\rho$  of the mover is constant, the mass and inertia-tensor elements of the mover are proportional to the third and fifth powers of a side of the mover, respectively. With this in mind, we can see that acceleration in the translational and rotational directions

becomes twice and four times, respectively, when all sides of the mover become half.

In this analytical model, two pairs of three-phase currents ( $i_{ju}$ ,  $i_{jv}$ , and  $i_{jw}$ ) shown in Fig. 3.3.1-2 are given as follows:

$$i_{ju} = I_j \sin(\theta_{sj}) \dots\dots\dots(3.3.1-5)$$

$$i_{jv} = I_j \sin\left(\theta_{sj} + \frac{2\pi}{3}\right) \dots\dots\dots(3.3.1-6)$$

$$i_{jw} = I_j \sin\left(\theta_{sj} + \frac{4\pi}{3}\right) \dots\dots\dots(3.3.1-7)$$

where  $I_j$  and  $\theta_{sj}$  are the amplitude and the phase of the three-phase currents, respectively. A phase difference between magnetic fields generated by the armature conductors and the mover can be defined as shown in Fig. 3.1.1-3 and expressed with the following equation:

$$\theta_{dj} = \theta_{sj} - \frac{\pi}{\tau} j_s \dots\dots\dots(3.3.1-8)$$

where  $x_s$  and  $y_s$  are the  $x$ - and  $y$ -positions of the mover center  $O'$  with respect to the stationary coordinate  $x_s, y_s, z_s$ . Controlling the amplitude  $I_j$  and phase  $\theta_{sj}$  of the armature conductors controls the 2-D mover motions.

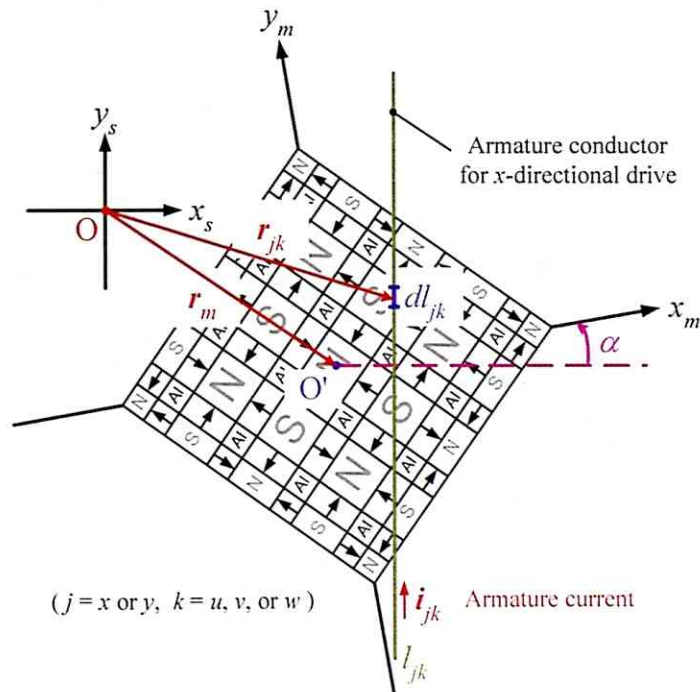


Fig. 3.3.1-1: Configuration of mover and stator in the analysis model.

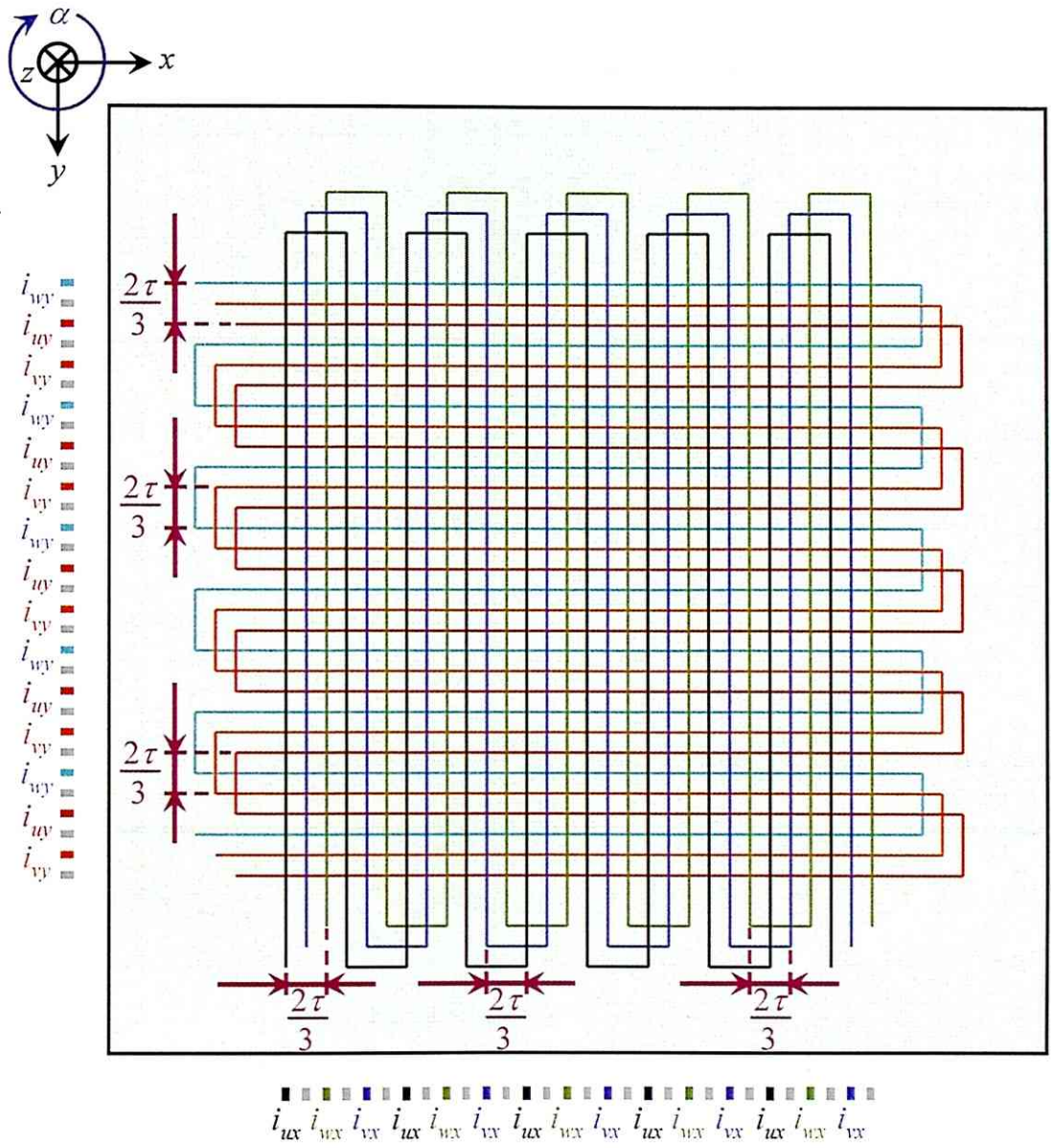
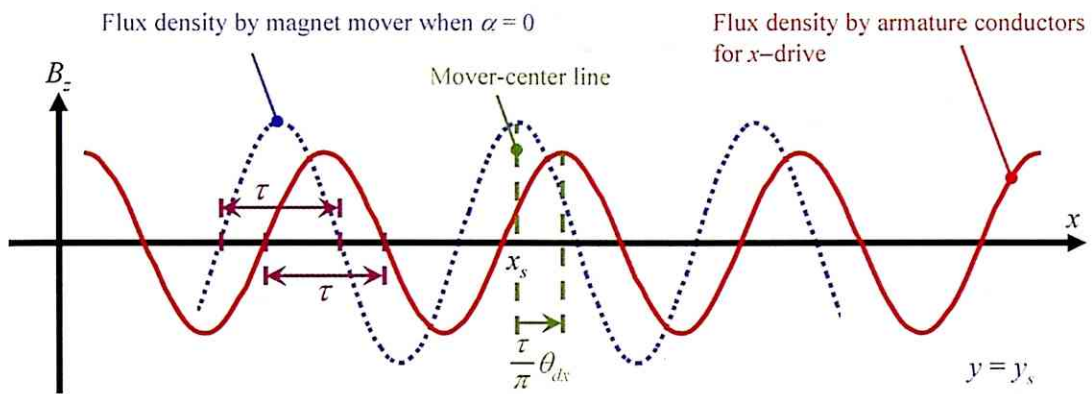
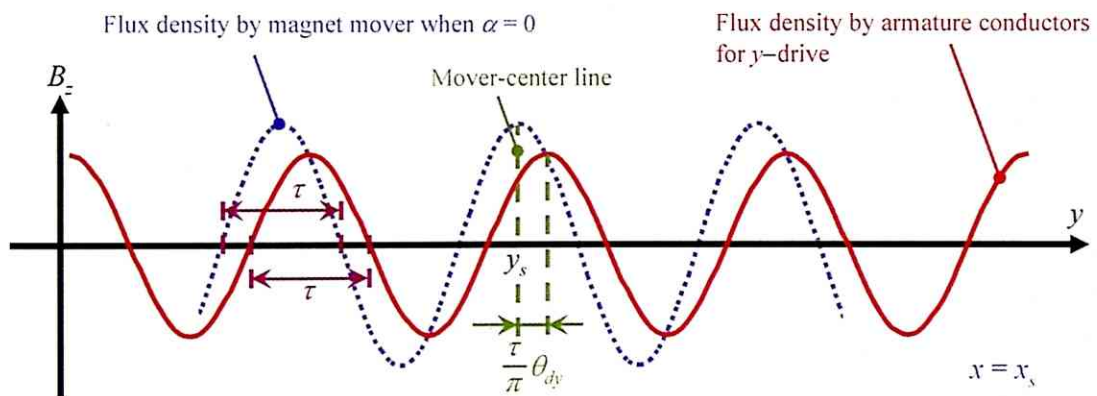


Fig. 3.3.1-2: Configuration of supplied armature currents.



(a) Phase difference for x-drive  $\theta_{dx}$ .



(b) Phase difference for y-drive  $\theta_{dy}$ .

Fig. 3.3.1-3: Definition of phase difference between magnetic fields generated by armature conductors and mover.

### 3.3.2. Numerical Analysis Results

Exciting the armature conductors for the  $x$ - and  $y$ -directional drives generates the  $x$ - and  $y$ -directional driving forces using the same principle, and so this analysis deals with the armature conductors for only the  $x$ -directional drive.

When the  $x_m$ - and  $y_m$ -axes are parallel to the stationary  $x_s$ - and  $y_s$ -axes, respectively, the yaw angle  $\alpha$  is defined to be 0 deg. Figure 3.3.2-1 shows a numerical analysis result of the translational force  $F_x$  and torque  $T_z$  for the phase difference  $\theta_{dx}$  with the following analysis conditions:

- amplitude of the armature currents:  $I_x = 2$  A,  $I_y = 0$  A
- phase of the armature currents:  $\theta_{dx} = -180 \sim 180$  deg
- mover position:  $x_s = 0$  mm
- yaw angle:  $\alpha = 10$  deg
- flux density due to the magnet mover: measurement result for air gap = 0.5 mm.

Figure 3.3.2-1 indicates that the translational force  $F_x$  and torque  $T_z$  can be expressed as sinusoidal functions with respect to the phase difference  $\theta_{dx}$ . Equations (3.3.1-3) and (3.3.1-4) also indicate the translational force  $F_x$  and torque  $T_z$  are proportional to the amplitude of the armature currents, and therefore can be expressed as follows:

$$F_x = K_{Fx}(\alpha)I_x \sin \theta_{dx} \dots\dots\dots(3.3.2-1)$$

$$T_z = K_{Tx}(\alpha)I_x \cos \theta_{dx} \dots\dots\dots(3.3.2-2)$$

These equations indicate that phases of the armature currents generating the translational force  $F_x$  and torque  $T_z$  differ by 90 deg. Furthermore, the armature currents generating a 90-deg phase-lead magnetic field with respect to the magnetic field due to the magnet mover ( $\theta_{dx} = 90$  deg) are proportional to the translational force  $F_x$ , and the armature currents generating the same-phase magnetic field ( $\theta_{dx} = 0$  deg) are proportional to the torque  $T_z$ . Figure 3.3.2-2 shows schematic views of the driving force generated by the armature currents generating 90-deg phase-lead or the same-phase magnetic fields.

The system constants  $K_{Fx}$  and  $K_{Tx}$  depend on the yaw angle  $\alpha$ . The system constants  $K_F$  and  $K_T$  can be calculated by fitting the analysis results of the driving forces to Eqs. (3.3.2-1) and (3.3.2-2). Figure 3.3.2-3 shows the calculation results of the system constants  $K_{Fx}$  and  $K_{Tx}$ . The same driving forces can be generated every 90 deg in the  $\alpha$ -direction because of the symmetric structure of the permanent-magnet mover. Figure 3.3.2-3 shows a period of the system constants  $K_{Fx}$  and  $K_{Tx}$  in the  $\alpha$ -direction. Figure

3.3.2-3 indicates that  $K_{f_x}$  is maximum and  $K_{T_x} = 0$  N·m/A when the yaw angle  $\alpha = 0$  deg, and so the translational force  $F_x$  is maximum and the torque  $T_z$  is not generated. When the mover is displaced in the  $\alpha$ -direction,  $K_{f_x}$  becomes smaller and  $K_{T_x} \neq 0$  N·m/A. The driving forces can be generated in the range within the yaw angle  $\alpha = \pm 30$  deg because of  $K_{f_x} \neq 0$  N/A and  $K_{T_x} \neq 0$  N·m/A. The movable area in the  $\alpha$ -direction is widest of all planar actuator having only two pairs of polyphase conductors. Therefore, this planar actuator is suitable for 3-DOF long-stroke planar manipulation using only a few conductors.

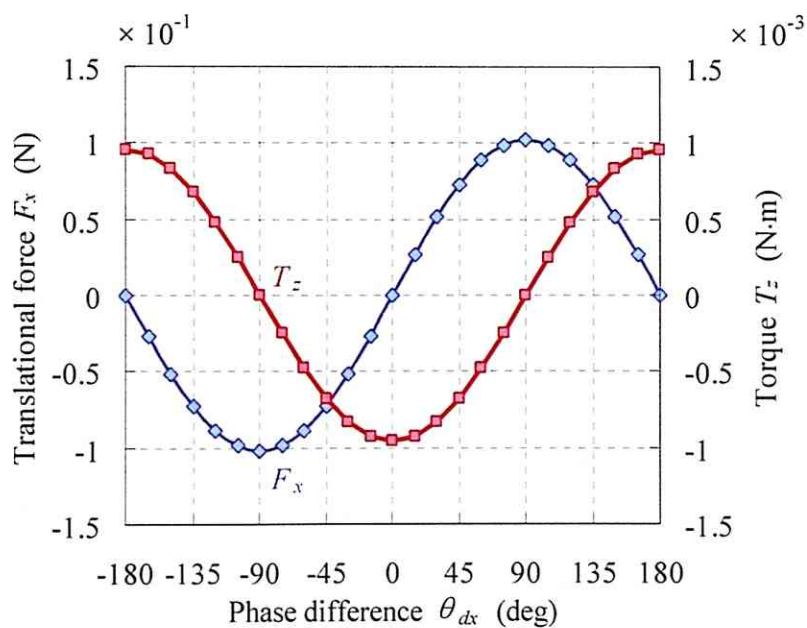
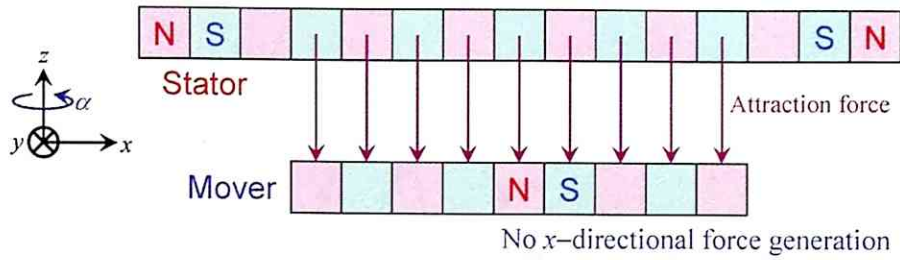
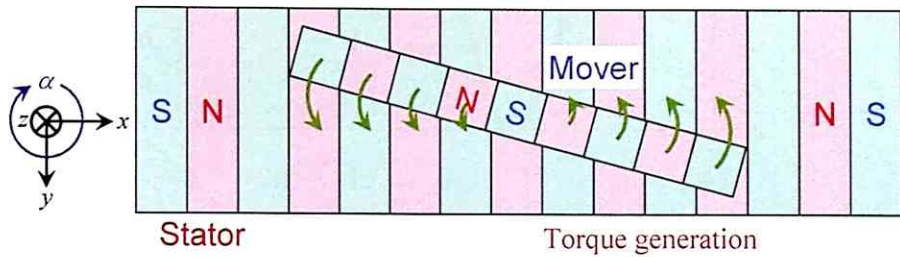


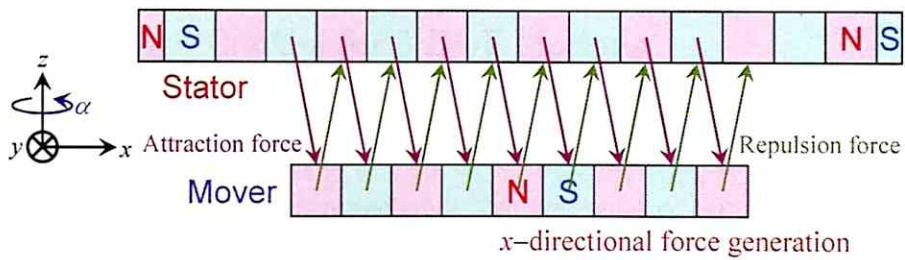
Fig. 3.3.2-1: Translational force  $F_x$  and torque  $T_z$  vs. phase difference  $\theta_{dx}$ .



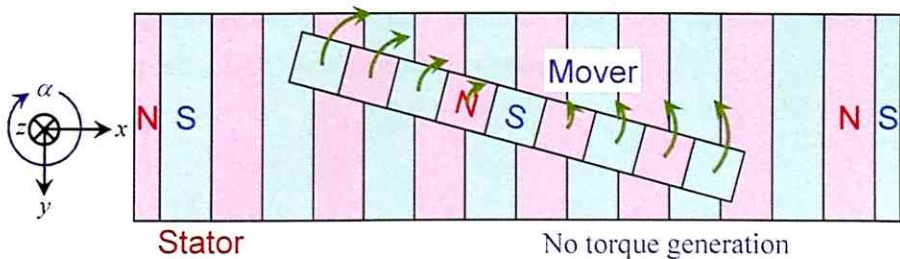
(a) Generated  $x$ -directional force when armature currents generating the same-phase magnetic field in the  $x$ -direction are supplied.



(b) Generated torque when armature currents generating the same-phase magnetic field in the  $x$ -direction are supplied.



(c) Generated  $x$ -directional force when armature currents generating 90-deg phase-lead magnetic field in the  $x$ -direction are supplied.



(d) Generated torque when armature currents generating 90-deg phase-lead magnetic field in the  $x$ -direction are supplied.

Fig. 3.3.2-2: Schematic views of driving force generation.

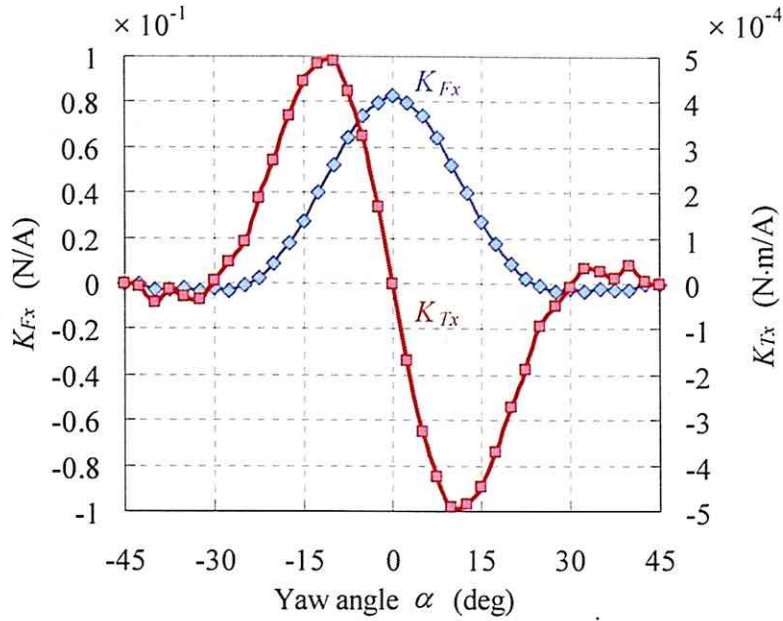


Fig. 3.3.2-3: System constants  $K_{F_x}$  and  $K_{T_x}$  vs. yaw angle  $\alpha$ .

### 3.4. Decoupled Control for 3-DOF Motions

This planar actuator was designed so that the 2-D Halbach permanent-magnet mover always faces the armature conductors for the  $x$ - and  $y$ -directional drives through 0.5-mm and 0.63-mm air gaps, respectively. The two types of armature conductors are structurally similar, and the phases of the armature currents generating the translational force  $F_x$  and torque  $T_x$  differ by 90 deg as shown in Eqs. (3.3.2-1) and (3.3.2-2). Therefore, DQ decomposition of the two kinds of armature currents expresses simply the relation between the driving forces and armature currents. This section introduces DQ decomposition of the two kinds of armature currents, and presents a design for a decoupled 3-DOF motion-control system.

#### 3.4.1. DQ Decomposition

DQ decomposition in conventional rotary machines separates armature-current components that are generating torques from those that are not [Fit90]. From preciously shown analysis results, DQ decomposition in this planar actuator separates

the armature-current components, generating the translational forces  $F_x$ ,  $F_y$  or torques  $T_z$ .

The direct axis ( $d$ -axis) and quadrature axis ( $q$ -axis) are attached to the mover, and move together with the mover. In a phasor diagram, conventionally, the  $d$ -axis is aligned with the magnetic field axis because of the permanent-magnet mover, and the  $q$ -axis leads the  $d$ -axis by 90 deg. In other words, the  $d$ -axis current is intended to generate the same-phase magnetic field as that resulting from the permanent-magnet mover, and the  $q$ -axis current is intended to generate a 90-deg phase-lead magnetic field. Figure 3.4.1-1 shows phasor diagrams for the relation between the  $dq$ -frame and  $uvw$ -frame. The  $u$ -,  $v$ -, and  $w$ -phase currents generate magnetic fields with definite phases, which are out of phase from one another by 120 deg. The  $\alpha'$ -axis current generates the same-phase magnetic field as that from the permanent-magnet mover when the mover center is at the origin of the stationary coordinate  $x_s y_s z_s$ . The  $\beta'$ -axis leads the  $\alpha'$ -axis by 90 deg. Figure 3.4.1-1 (b) indicates that the  $u$ -,  $v$ -, and  $w$ -axis components are easily decomposed to the  $\alpha'$ - and  $\beta'$ -axis components. Figure 3.4.1-1 (a) indicates that the  $d$ - and  $q$ -axes lead the  $\alpha'$ - and  $\beta'$ -axes by  $(\pi j_s / \tau)$ , respectively, which is proportional to the mover positions  $j_s$  ( $= x_s$  or  $y_s$ ). The armature currents having the amplitude  $I_j$  and phase  $\theta_{dj}$  can be decomposed to the  $d$ -axis currents  $I_{dj}$  and  $q$ -axis currents  $I_{qj}$  as follows:

$$I_{dj} = I_j \sin \theta_{dj} \dots\dots\dots (3.4.1-1)$$

$$I_{qj} = I_j \cos \theta_{dj} \dots\dots\dots (3.4.1-2)$$

From Eqs. (3.3.2-1), (3.3.2-2), (3.4.1-1) and (3.4.1-2), the translational forces  $F_x$ ,  $F_y$  and torques  $T_z$  resulting from supplying the two pairs of three-phase currents to the armature conductors for the  $x$ - and  $y$ -directional drives, can be expressed with the  $d$ - and  $q$ -axis currents  $I_{dj}$ ,  $I_{qj}$  as follows:

$$F_x = K_{Fx}(\alpha) I_{qx} \dots\dots\dots (3.4.1-3)$$

$$F_y = K_{Fy}(\alpha) I_{qy} \dots\dots\dots (3.4.1-4)$$

$$T_z = K_{Tx}(\alpha) I_{dx} + K_{Ty}(\alpha) I_{dy} \dots\dots\dots (3.4.1-5)$$

Equations (3.4.1-3), (3.4.1-4), and (3.4.1-5) indicate that the translational forces  $F_x$ ,  $F_y$  and torques  $T_z$  are proportional to the  $q$ - and  $d$ -axis currents  $I_{qj}$ ,  $I_{dj}$ , respectively. The system constants for the  $y$ -directional drive  $K_{Fy}$ ,  $K_{Ty}$  are slightly different from those for the  $x$ -directional drive  $K_{Fx}$ ,  $K_{Tx}$  because of difference in the air gaps between the mover and armature conductors for the  $x$ - or  $y$ -directional drives. As mentioned above, the driving forces from the armature currents can be simply described. Figure 3.4.1-2 shows the  $dq$ -frame and  $\alpha'\beta'$ -frame for the  $x$ - and  $y$ -directional drives.



### 3.4.2. 3-DOF Force Control

Supplying the appropriate  $d$ - and  $q$ -axis currents independently controls the translational forces  $F_x$ ,  $F_y$  and torques  $T_z$  from Eqs. (3.4.1-3)–(3.4.1-5). The degrees of freedom for the armature-current controls are four ( $I_{dx}$ ,  $I_{dy}$ ,  $I_{qx}$ , and  $I_{qy}$ ), and one larger than that for the mover motions, which is three ( $x$ ,  $y$ , and  $\alpha$ ) as shown in Fig. 3.4.2-1. Controlling the two  $q$ -axis currents  $I_{qx}$ ,  $I_{qy}$  is essential to controlling the two translational forces  $F_x$ ,  $F_y$ . The two  $d$ -axis currents  $I_{dx}$ ,  $I_{dy}$  generate the torques  $T_z$ , and, so the torque controls have redundancy. In fact, the  $d$ -axis current  $I_{dx}$  generates the torques  $T_z$  more efficiently than the  $d$ -axis current  $I_{dy}$  because of the air-gap difference ( $K_{Tx} > K_{Ty}$ ). However, each armature current is limited by its own rating, power supply, and so on, as follows:

$$I_c \geq |I_j| = \sqrt{I_{dj}^2 + I_{qj}^2} \dots\dots\dots(3.4.2-1)$$

where  $I_c$  is the current limit of all the armature currents. So if large driving forces  $F_x$ ,  $F_y$ ,  $T_z$  are required, then armature currents should be supplied so as to optimally satisfy the references of the driving forces under the current limit for producing maximum performance. This study, however, focuses principally on the verification of decoupled 3-DOF motion controls for a long-stroke planar actuator, and, therefore deals with a simply decoupled control algorithm.

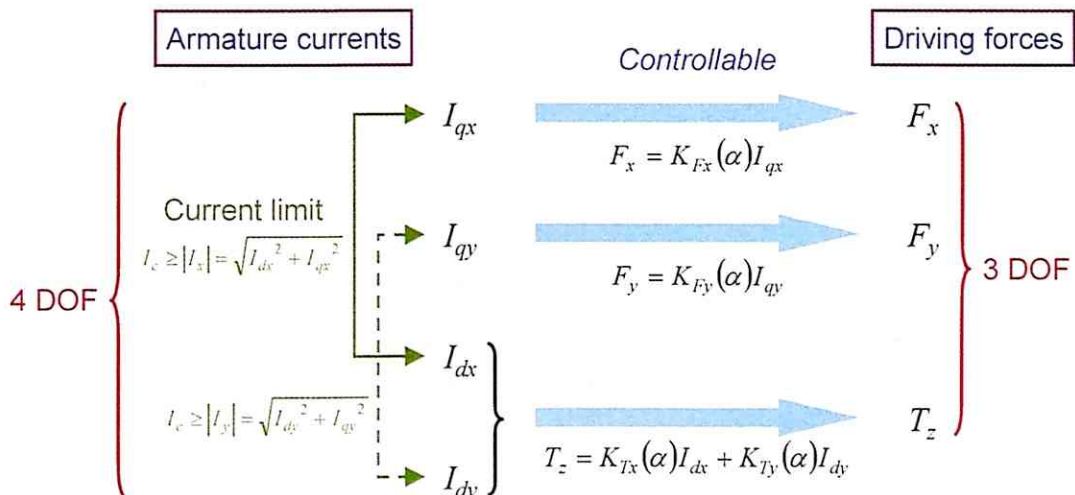


Fig. 3.4.2-1: Degrees of freedom for armature-current control and mover motion.

Figure 3.4.2-2 shows a control block diagram for the translational forces  $F_x$ ,  $F_y$  and torques  $T_z$  in this study. In Fig. 3.4.2-2,  $x_{ref}$ ,  $y_{ref}$ , and  $\alpha_{ref}$  are references of the mover positions in the  $x$ -,  $y$ -, and  $\alpha$ -directions, respectively. In order to decide the references for the driving forces  $F_x^*$ ,  $F_y^*$ ,  $T_z^*$ , feedback controls in each degree of freedom are performed with three different PID (Proportional-Integral-Derivative) algorithms. The PID parameters are determined so that settling time of the  $x$ -,  $y$ -, and  $\alpha$ -directional drives is shorter than 0.5 s. In this study, references of the  $d$ - and  $q$ -axis currents  $I_{dj}^*$ ,  $I_{qj}^*$  are calculated from the system constants  $K_{Fj}$ ,  $K_{Tj}$  and the driving force references  $F_x^*$ ,  $F_y^*$ ,  $T_z^*$  as follows ( $j = x$  or  $y$ );

$$I_{dj}^* = \frac{T_z^*}{2K_{Tj}(\alpha)} \dots\dots\dots(3.4.2-2)$$

$$I_{qj}^* = \frac{F_j^*}{K_{Fj}(\alpha)} \dots\dots\dots(3.4.2-3)$$

The system constants  $K_{Fj}$ ,  $K_{Tj}$  are calculated from the detected yaw angle  $\alpha$  by interpolation of the analysis data shown in Fig. 3.3.2-3. As we can see from Fig. 3.4.1-1, the references of the amplitude and phase of the three-phase currents  $I_j^*$  and  $\theta_{sj}^*$  can be calculated from the current references in the  $dq$ -frame  $I_{dj}^*$ ,  $I_{qj}^*$  and the mover positions in the  $x$ - and  $y$ -directions as follows;

$$I_j^* = \sqrt{(I_{dj}^*)^2 + (I_{qj}^*)^2} \dots\dots\dots(3.4.2-4)$$

$$\theta_{sj}^* = \theta_{dj}^* + \frac{\pi}{\tau} j_s \dots\dots\dots(3.4.2-5)$$

$$\theta_{dj} = \begin{cases} \tan^{-1}\left(\frac{I_{qj}^*}{I_{dj}^*}\right) & (I_{dj}^* \geq 0) \\ \tan^{-1}\left(\frac{I_{qj}^*}{I_{dj}^*}\right) + \pi & (I_{dj}^* < 0) \end{cases} \dots\dots\dots(3.4.2-6)$$

References of the three-phase currents  $i_{ju}^*$ ,  $i_{jv}^*$ ,  $i_{jw}^*$ , ( $j = x$  or  $y$ ) can be calculated from the amplitude  $I_j^*$  and phase  $\theta_{sj}^*$  as follows;

$$i_{ju}^* = I_j^* \sin(\theta_{sj}^*) \dots\dots\dots(3.4.2-7)$$

$$i_{jv}^* = I_j^* \sin\left(\theta_{sj}^* + \frac{2\pi}{3}\right) \dots\dots\dots(3.4.2-8)$$

$$i_{jw}^* = I_j^* \sin\left(\theta_{sj}^* + \frac{4\pi}{3}\right) \dots\dots\dots(3.4.2-9)$$

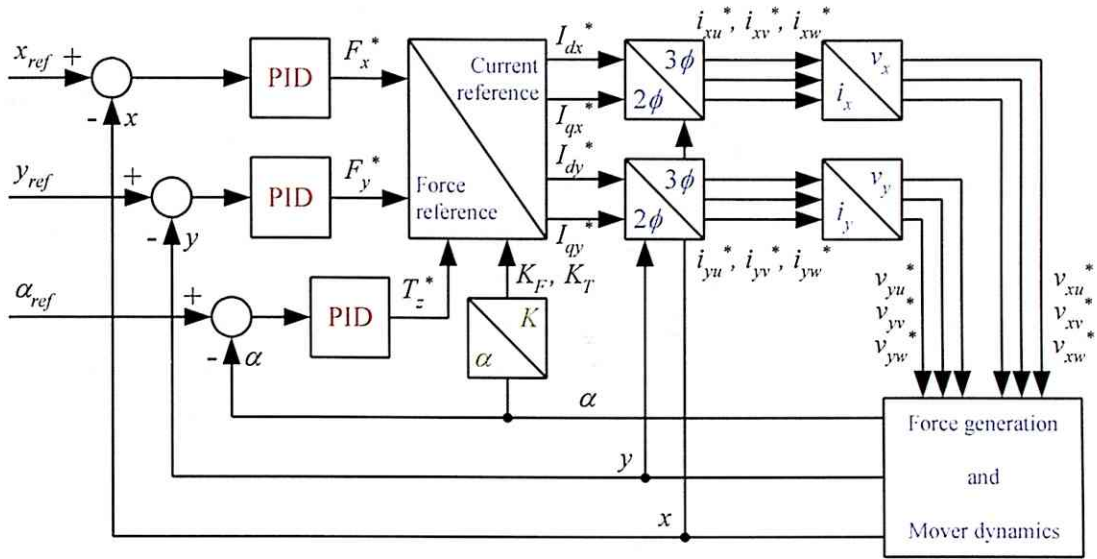


Fig. 3.4.2-2: Control block diagram for translational forces  $F_x$ ,  $F_y$  and torques  $T_z$ .

In this study, each phase armature voltage  $v_{jk}^*$  is calculated from the resistances  $R$  and armature-current references  $i_{jk}^*$  as follows:

$$v_{jk}^* = Ri_{jk}^* \dots\dots\dots (3.4.2-10)$$

Equation (3.4.2-10) does not consider back electromotive force, and causes errors between the armature currents and their references. In this study, the errors are compensated by the PID controls. As described above, the six armature-voltage references  $v_{jk}^*$  can be calculated from the driving force references  $F_x^*$ ,  $F_y^*$ ,  $T_z^*$ . Supplying the six armature voltages  $v_{jk}^*$  generates decoupled 3-DOF driving forces.

### 3.5. Summary of Chapter 3

This chapter proposed a novel synchronous planar actuator with spatially superimposed magnetic circuits for the  $x$ - and  $y$ -dimensional drives by the combination of a 2-D Halbach permanent-magnet mover and overlapped stationary armature conductors. A planar actuator with moving magnets has advantages in terms of the wide movable area of the mover, which is independent of the number of armature conductors. Numerical analysis results of the driving forces indicate that the translational forces  $F_x$ ,  $F_y$  and torques  $T_z$  depend on the yaw angle  $\alpha$ , and, so the

$\alpha$ -motions are required to be also controlled to drive the mover in the  $x$ - and  $y$ -directions on a plane. To separate the armature-current components generating the translational forces  $F_x$ ,  $F_y$ , or torques  $T_z$ , the armature currents were decomposed to the  $dq$ -frame. Analysis results indicate that the  $q$ - and  $d$ -axis currents generate translational forces  $F_x$ ,  $F_y$ , and torques  $T_z$ , respectively. Then, a decoupled control law for 3-DOF motion of the mover can be designed.

Next, in order to experimentally investigate the drive characteristics of my proposed planar actuator, by fabricating an experimental system for instance, a position-sensing system and a mover-suspension-and-guide mechanism are necessary.

## Chapter 4

# Design of Experimental System for Long-Stroke Planar Actuator

This chapter presents the design for an experimental system for the verification of the motion-control characteristics of the planar actuator.

## 4. Design of Experimental System for Long-Stroke Planar Actuator

This chapter presents the design of the experimental system for my proposed long-stroke planar actuator to verify the drive characteristics of the mover. The experimental system can be classified as the position-sensing system, mover-suspension-and-guide mechanism, controller, and power supply.

### 4.1. Experimental Setup

This section lists the configuration of the experimental system and the specifications of the experimental apparatuses utilized.

#### 4.1.1. Configuration of Experimental System

In order to control the 3-DOF ( $x$ ,  $y$ , and  $\alpha$ ) motions of the mover by position feedback, sensing the mover positions is extremely important. If multiple sensors are utilized for single-axis displacements, we require three or more sensors to detect the 3-DOF positions. The combination method for multiple sensors determines the measurement performance, for instance, detection accuracy and measurable area, and so is also extremely important. This study uses three single-axis laser-displacement sensors (laser triangulation) because of their long measurable area (several tens of mm) and high resolution (several  $\mu\text{m}$ ).

When the mover is driven in 3-DOF directions, suspending and smoothly guiding the mover on a plane are also extremely important. This study uses ball bearings, 1-mm glass spheres, as the suspension and guide mechanism because they have smaller friction forces and are easily installed.

Figures 4.1.1-1 and 4.1.1-2 show the configuration of the experimental system for the 3-DOF motion controls of the mover, and the fabricated experimental system. The mover is supported by many ball bearings and guided on a plane having small frictional forces. At the same time, the mover faces the three-phase armature conductors for the  $x$ - and  $y$ -directional drives through 0.5-mm and 0.63-mm air gaps, respectively. The air gap can be precisely adjusted by the 10- $\mu\text{m}$ -resolution  $z$ -axis stage, which is fixed with a

top plate, from are suspended the stationary armature conductors. The three laser-displacement sensors irradiate three points on three lateral sides of the mover, and detect displacements at the three points by triangulation. A personal computer (PC), running a Digital Signal Processor (DSP), and Analog-to-Digital A/D (A/D) and Digital-to-Analog (D/A) converter boards, inputs the three sensor signals and calculates the 3-DOF positions of the mover. The PC also calculates the six armature-voltage references based on a decoupled motion-control algorithm, and outputs the six voltages to the six armature conductors through the power amplifiers. Then, the armature currents and magnetic field, resulting from the magnet mover, interact and independently controlled driving forces are generated.

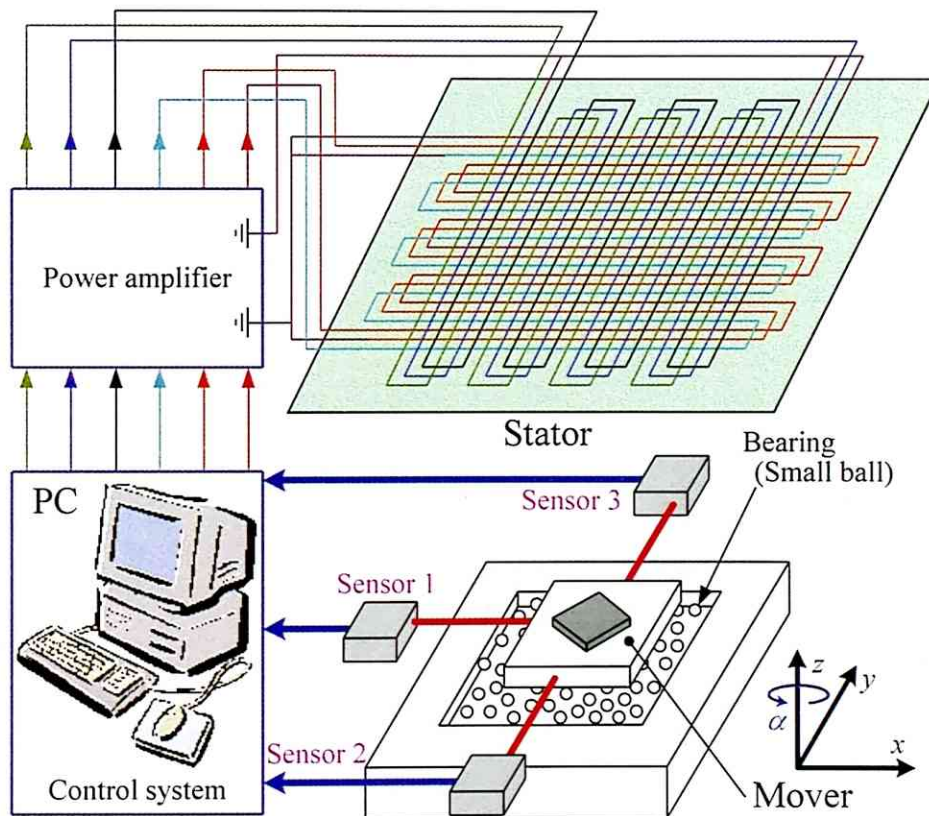
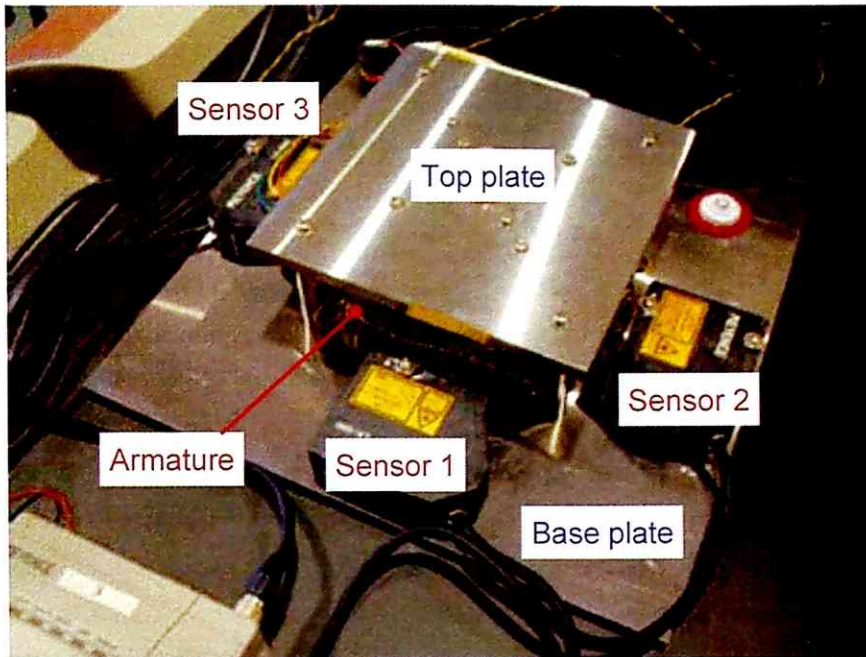
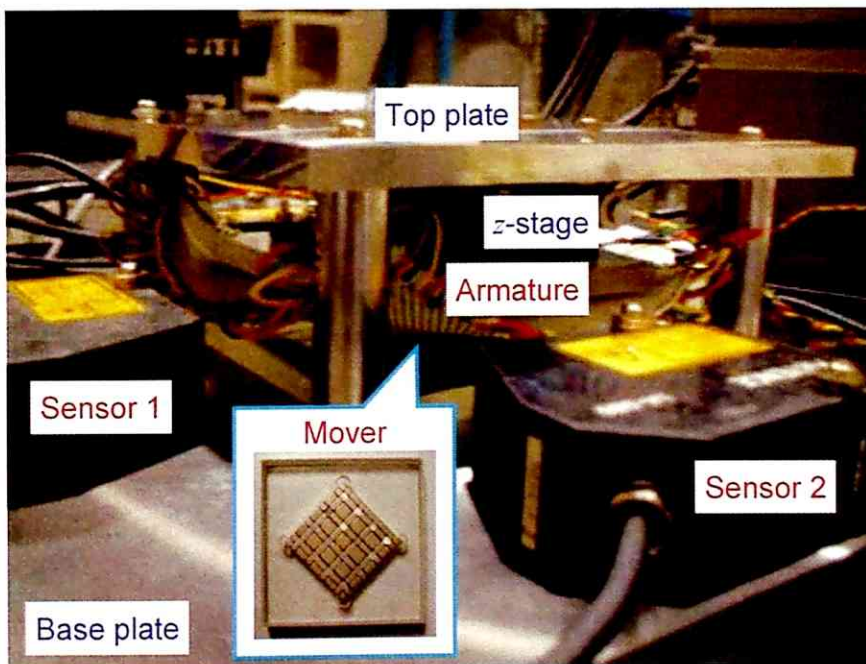


Fig. 4.1.1-1: Configuration of experimental system for 2-D drives.



(a) Top view of experimental system.



(b) Side view of experimental system.

Fig. 4.1.1-2: Fabricated experimental system for 2-D drives.

#### 4.1.2. Experimental Apparatuses

This section presents the specifications of the experimental apparatuses for the 2-D drives.

##### Laser-displacement sensor [Key01]

A laser-displacement sensor for the measurement of single-axis displacements using a 670-nm laser diode and a CCD (Charge-Coupled Device) array (Keyence LK-080) is used to detect the mover positions in the experiments. In the laser-displacement sensor, imaging diffusely or specularly reflected light on the measurement surface with the CCD array measures the distance between the sensor head to the measurement point by means of laser triangulation. The measurable area is wide, within a range of  $\pm 15$ -mm displacement at a distance of 80 mm. The laser-displacement sensor has a resolution of 3  $\mu\text{m}$  and outputs 3 V per 1-mm displacement every 1024- $\mu\text{s}$  sampling time.

If the reflected light to be imaged using the CCD array is intense, a sensor output with a high Signal-to-Noise Ratio (SNR) is obtained. In this study, white tapes were attached to the lateral sides of the mover, corresponding to the measurement surfaces, so as to generate intense reflected light to obtain high-SNR measurement signals.

##### DSP [MTT01]

A Texas Instruments digital signal processor (TMS320C6701) is used to digitally implement the motion-control algorithms in the experiment. The operational frequency and total memory space of the DSP are 167 MHz and 6 MB, respectively. The processor is connected to A/D and D/A converter boards.

##### A/D and D/A Converter Boards [MTT02, MTT03]

A Texas Instruments 16-bit 4-channel simultaneous-conversion A/D converter module (ADS7805U) is used to input the three output signals of the laser-displacement sensors in the experiment. The A/D converter module has  $\pm 10$ -V input-voltage range, 100-k $\Omega$  input impedance, and 100-kHz maximum conversion frequency.

An Analog Devices 12-bit 8-channel simultaneous-conversion D/A converter module (DAC8412PC) is used to output six voltage signals to the six armature conductors in the experiment. The D/A converter module has a  $\pm 10$ -V output-voltage range, less than 1- $\Omega$

output impedance, 120-kHz maximum conversion frequency, and 100-kHz first-order low-pass filter.

### Power amplifiers

Six power amplifiers, through which six voltages are supplied to the armature conductors in the experiment, were manufactured by Asst. Prof. Minoru Tamura of The University of Tokyo. Figure 4.1.2-1 shows the circuit configuration of the power amplifier for an armature conductor. The power amplifier consists of a Texas Instruments operational amplifier (OPA 548) [Tex01] and a negative feedback circuit including resistance and capacitance elements. The output current of the power amplifier is measured with a LEM current sensor (LA 55-P) [LEM01]. The power amplifier has the following specifications:

- voltage gain =  $\times 3$
- input-voltage range =  $\pm 5$  V
- output voltage range =  $\pm 15$  V
- current capacity = 3 A
- cutoff frequency = 100 kHz.

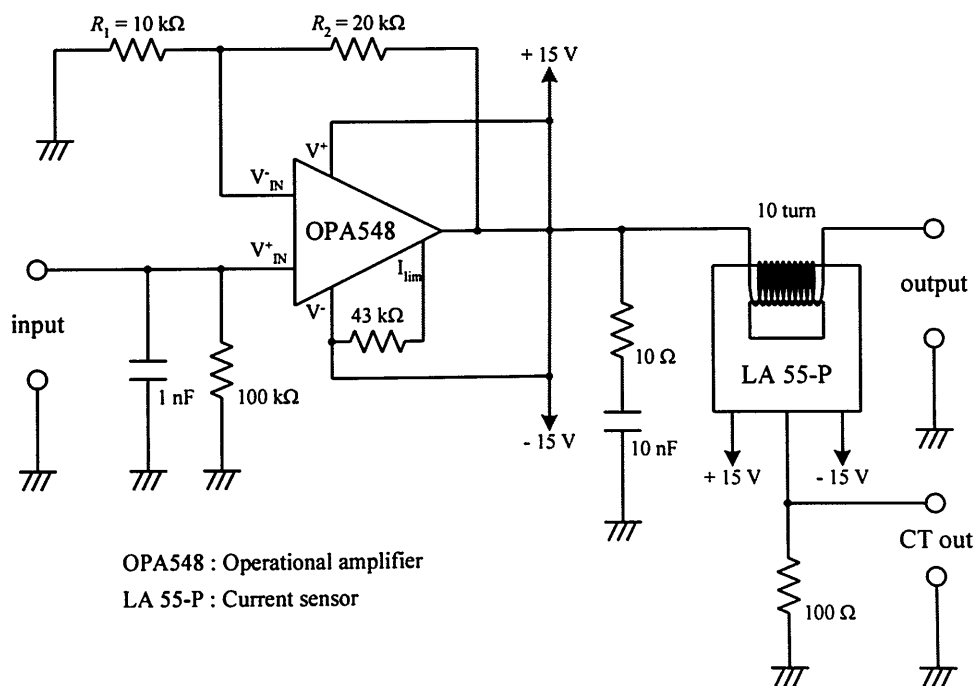


Fig. 4.1.2-1: Circuit configuration of power amplifier for an armature conductor.

## 4.2. 3-DOF Position Sensing

As mentioned in Subsection 1.2.3, various methods for MDOF position sensing have been proposed. The mover that this study uses is extremely small (several tens of mm), and is designed to travel over 3-DOF large displacements on a plane. Position-sensing methods of the mover using lasers can be easily realized because of the long path (far in excess of 100 mm) and small spot (less than 1 mm) of lasers. Laser interferometers can measure positions of a point on a mirror surface orthogonal to the laser at a very high resolution (less than 1 nm) by detecting the intensity of the interfering light between specularly reflected light and incident light. However, laser interferometers cannot measure on the surface nonorthogonal to the laser because the interference does not occur. In this study, three laser-displacement sensors, which can measure positions by laser triangulation, are used to detect 3-DOF positions regardless of the angles between incident light and measurement surface. This section describes the sensing method of the 3-DOF mover positions.

### 4.2.1. Alignment of Sensors

Figure 4.2.1-1 shows the alignment of the three laser-displacement sensors for position sensing with 3 DOF ( $x$ ,  $y$ , and  $\alpha$ ). The 3-DOF positions are obtained in the following order:

- yaw-angle ( $\alpha$ ) calculation from two laser-displacement sensors, Sensor 2 and Sensor 3
- $x$ - and  $y$ -position calculation from yaw angle  $\alpha$  and Sensor 1 (or Sensor 2).

In Fig. 4.2.1-1, origin O is defined to be on both the axis of Sensor 1 and the center of the axes of Sensor 2 and Sensor 3. The output signals of the three laser-displacement sensors  $S_1$ ,  $S_2$ ,  $S_3$ , which are commuted from voltage signals (V) to position signals (mm), can be expressed by relative positions among the laser-displacement sensors  $x_{12}$ ,  $y_{12}$ ,  $x_{23}$ ,  $y_{23}$  as follows;

$$S_1 = X_1 + \frac{x_{23}}{2} + x_{12} - D \dots\dots\dots(4.2.1-1)$$

$$S_2 = Y_2 + y_{12} - D \dots\dots\dots(4.2.1-2)$$

$$S_3 = -Y_3 + y_{23} - y_{12} - D \dots\dots\dots(4.2.1-3)$$

where  $S_1$ ,  $S_2$ , and  $S_3$  express displacements between sensor heads and measurement points  $X_1$ ,  $Y_2$ , and  $Y_3$  for the reference distance  $D = 80$  mm, respectively.

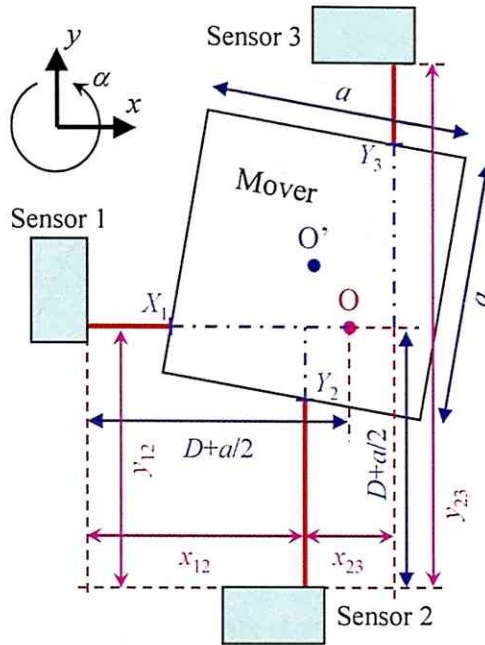


Fig. 4.2.1-1: Alignment of three laser-displacement sensors.

#### 4.2.2. Measurable Area for Mover Position

In this study, the parameters shown in Fig. 4.2.1-1 are set as follows; one side of the square mover  $a = 60$  mm, and the relative positions among the laser-displacement sensors  $x_{12} = 100$  mm,  $y_{12} = 110$  mm,  $x_{23} = 20$  mm,  $y_{23} = 220$  mm. Figure 4.2.2-1 shows the theoretical output signals of the three sensors  $S_1$ ,  $S_2$ ,  $S_3$  for the yaw angle  $\alpha$  at  $(x, y) = (0, 0)$ , which can be obtained by Eqs. (4.2.1-1), (4.2.1-2), and (4.2.1-3). The obtained output signals have a 90-deg periodicity for the yaw angle  $\alpha$  because of the square structure of the mover. Summation of the output signals ( $S_2 + S_3$ ) is maximum or minimum at the yaw angle  $\alpha = \alpha_{\min}$  or  $\alpha = \alpha_{\max}$ , respectively, and the measurement points at  $(x, y) = (0, 0)$  are shown in Fig. 4.2.2-2. The yaw angles  $\alpha_{\min}$  and  $\alpha_{\max}$  can be expressed as follows:

$$\alpha_{\min} = -\sin^{-1}\left(\frac{x_{23}}{a}\right) \dots\dots\dots (4.2.2-1)$$

$$\alpha_{\max} = 45 - \sin^{-1}\left(\frac{x_{23}}{\sqrt{2}a}\right) \dots\dots\dots (4.2.2-2)$$

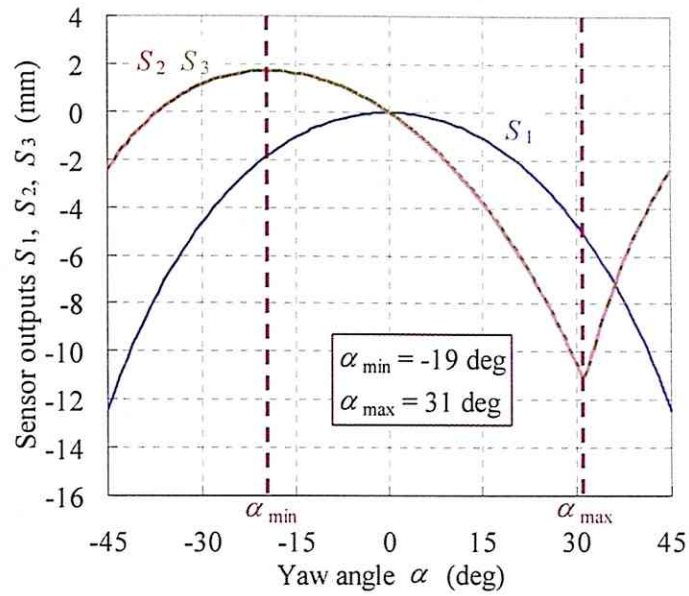
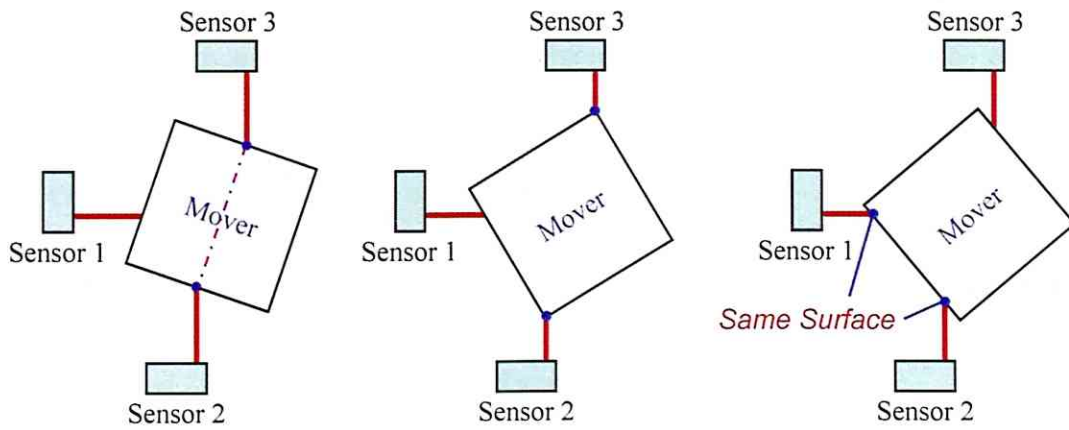


Fig. 4.2.2-1: Theoretical output signals of the three sensors  $S_1$ ,  $S_2$ ,  $S_3$  for the yaw angle  $\alpha$  at  $(x, y) = (0, 0)$ .



(a) Yaw angle  $\alpha = \alpha_{\min}$ . (b) Yaw angle  $\alpha = \alpha_{\max}$ . (c) Same surface irradiated.

Fig. 4.2.2-2: Irradiated positions by laser-displacement sensors at  $(x, y) = (0, 0)$ .

Figure 4.2.2-1 shows that there are the same sensor outputs  $S_2$  and  $S_3$  at the two different yaw angles in the range within the yaw angle  $\alpha = \pm 45$  deg, and that the yaw angle  $\alpha$  cannot be uniquely obtained from sensor outputs  $S_2$  and  $S_3$ , in principle, in this range. In the case of the mover positions  $(x, y) \neq (0, 0)$ , the yaw angle  $\alpha$  also cannot be uniquely obtained from sensor outputs  $S_2$  and  $S_3$ . Therefore in this study, the 3-DOF positions are limited to the range between  $\alpha = \alpha_{\min}$  and  $\alpha = \alpha_{\max}$  to be measured. The yaw angles  $\alpha_{\min}$  and  $\alpha_{\max}$  are dependent on the  $x$ - and  $y$ -positions, and in the case of mover positions  $(x, y) = (0, 0)$ , the range between  $\alpha_{\min}$  and  $\alpha_{\max}$  is maximum.

Furthermore, if Sensor 1 and Sensor 2 (or Sensor 3) irradiate the same surface as shown in Fig. 4.2.2-2 (c), the  $x$ - and  $y$ -positions of the mover cannot be obtained (only the  $\alpha$ -position can be obtained).

Therefore, the 3-DOF positions of the mover can be uniquely obtained from the output signals of the three laser-displacement sensors under the following conditions:

- yaw angle  $\alpha$ :  $\alpha_{\min} < \alpha < \alpha_{\max}$
- there are three different surfaces irradiated by Sensor 1, Sensor 2, and Sensor 3.

### 4.2.3. Calculation of Mover Position

When the yaw angle  $\alpha$  is in the range within  $\alpha_{\min} < \alpha < \alpha_{\max}$  and the three laser-displacement sensors irradiate three different surfaces, the yaw angle  $\alpha$  can be calculated from a side of mover  $a$ , the measurement positions  $Y_2$ ,  $Y_3$ , and the relative position between Sensor 2 and Sensor 3  $x_{23}$  as follows:

$$\alpha = -\sin^{-1}\left(\frac{a}{\sqrt{x_{23}^2 + (Y_3 - Y_2)^2}}\right) + \tan^{-1}\left(\frac{Y_3 - Y_2}{x_{23}}\right) \dots\dots\dots(4.2.3-1)$$

where  $Y_2$  and  $Y_3$  can be calculated from the sensor outputs  $S_2$  and  $S_3$  by Eqs. (4.2.1-2) and (4.2.1-3), respectively. Then, the  $x$ - and  $y$ -positions can be calculated from the sensor outputs  $S_1$  and  $S_2$  (or  $S_3$ ), and the obtained yaw angle  $\alpha$  as follows:

$$x = X_1 \cos^2 \alpha - \frac{x_{23}}{2} \sin^2 \alpha - Y_2 \cos \alpha \sin \alpha + \frac{a}{2} (\cos \alpha - \sin \alpha) \dots\dots\dots(4.2.3-2)$$

$$y = \left(X_1 + \frac{x_{23}}{2}\right) \cos \alpha \sin \alpha + Y_2 \cos^2 \alpha + \frac{a}{2} (\cos \alpha + \sin \alpha) \dots\dots\dots(4.2.3-3)$$

Figure 4.2.3-1 shows the theoretically calculated mover positions  $x$ ,  $y$ , and  $\alpha$  from the theoretical sensor outputs  $S_1$ ,  $S_2$ , and  $S_3$  at  $(x, y) = (0, 0)$ , shown in Fig. 4.2.2-1, by Eqs.

(4.2.3-1), (4.2.3-2), and (4.2.3-3). Figure 4.2.3-1 shows that the 3-DOF positions of the mover can be correctly detected when the yaw angle  $\alpha$  is in the range within  $\alpha_{\min} < \alpha < \alpha_{\max}$ .

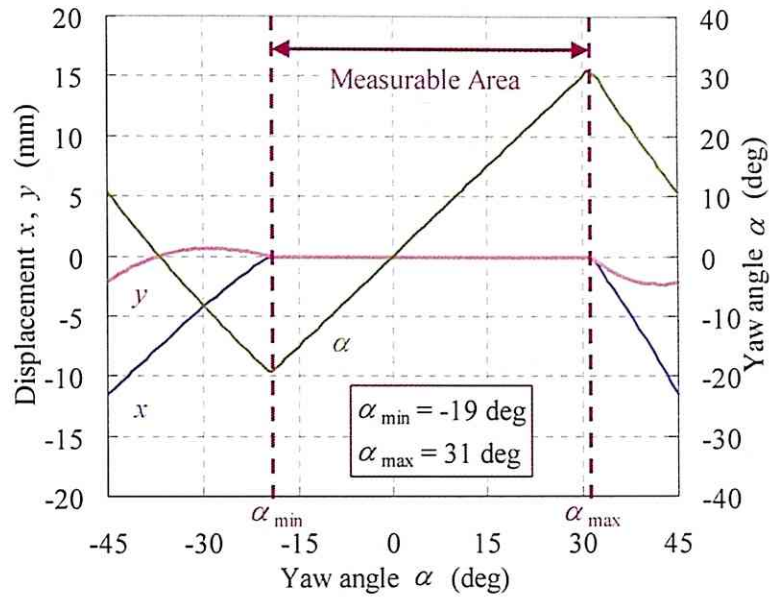


Fig. 4.2.3-1: Theoretical calculated mover positions  $x$ ,  $y$ , and  $\alpha$  for the yaw angle  $\alpha$  at  $(x, y) = (0, 0)$ .

#### 4.2.4. Position-Sensing Test

The position sensing of the mover positions was tested to verify this position-sensing method after the alignment of the three laser-displacement sensors as shown in Fig. 4.2.4-1. A measured object, the same size as the mover, was attached to the 10-mm-and-10'-resolution  $xyz\alpha$ -axis stage. In this test, the measured object was always positioned at  $(x, y) = (0, 0)$  by the  $xyz\alpha$ -axis stage. Figure 4.2.4-2 shows the experimentally obtained sensor outputs of the three laser-displacement sensors for the yaw angle  $\alpha$ . Comparing Fig. 4.2.4-2 with Fig. 4.2.2-1, the experimental results of the sensor outputs are almost in agreement with the theoretical results within an error range of  $\pm 1$  mm. Figure 4.2.4-3 shows detected mover positions at  $(x, y) = (0, 0)$  for the yaw angle  $\alpha$ . Figures 4.2.4-3 and 4.2.3-1 indicate that the mover positions can be experimentally detected in a wide measurable area,  $-15 \text{ deg} < \text{the yaw angle } \alpha < 32 \text{ deg}$ ,

with less than 0.3-mm and 1-deg errors. The measurable area is enough wide for a planar actuator capable of generating sufficient driving forces in the range within the yaw angle  $\alpha \approx \pm 30$  deg. The slight errors are presumed to be caused by alignment errors and temperature drift arising from laser-displacement errors.

### 4.3. Summary of Chapter 4

This chapter presents the design for the experimental system for verification of the drive characteristics of my proposed long-stroke planar actuator. In this study, the mover is suspended and guided by ball bearings because they offer less friction force. The 3-DOF mover positions are detected using three laser-displacement sensors, and the position sensing was tested. The test results indicate that the mover positions can be detected in a sufficiently wide measurable area,  $-15 \text{ deg} < \text{the yaw angle } \alpha < 32 \text{ deg}$ , with 0.3-mm and 1-deg accuracies. In the next step, it is required that the drive characteristics of the planar actuator be verified by experimental study.

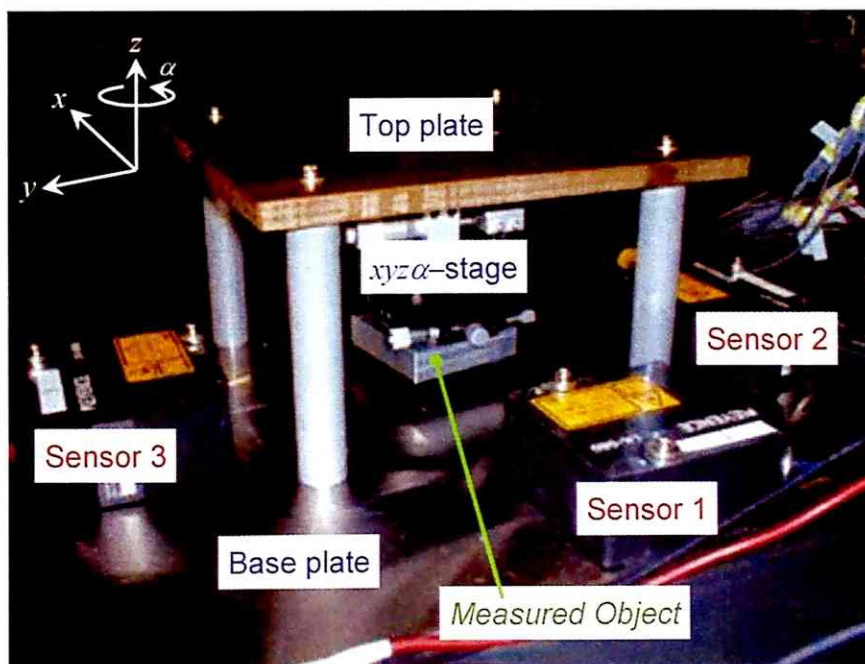


Fig. 4.2.4-1: Configuration of experimental apparatuses for the position-sensing test.

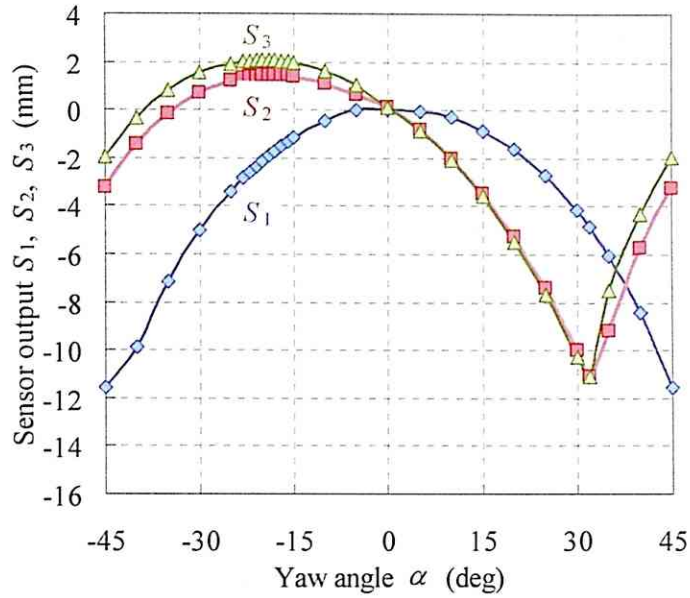


Fig. 4.2.4-2: Experimentally obtained sensor outputs of the three sensors  $S_1$ ,  $S_2$ ,  $S_3$  at  $(x, y) = (0, 0)$  for the yaw angle  $\alpha$ .

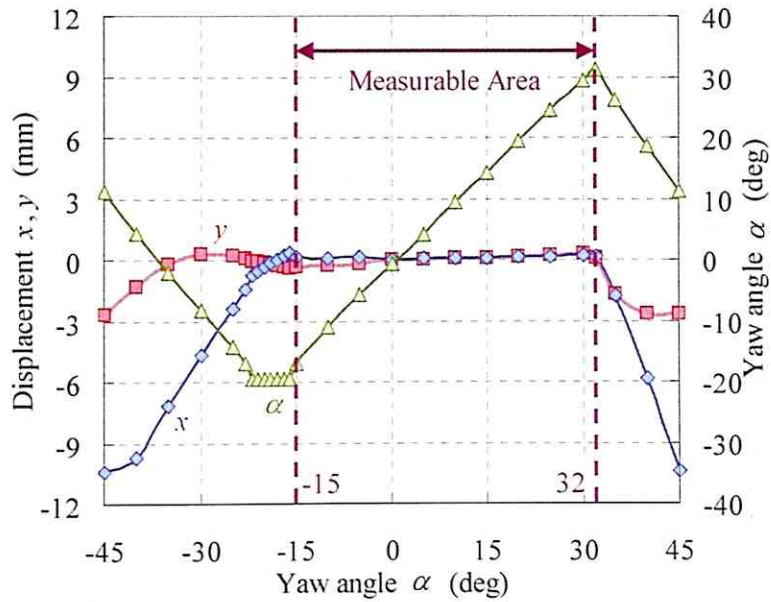


Fig. 4.2.4-3: Detected mover positions  $x$ ,  $y$ ,  $\alpha$  at  $(x, y) = (0, 0)$  for yaw angle  $\alpha$ .

## Chapter 5

# Experimental Motion Control of Long-Stroke Planar Actuator

This chapter describes the experimental results of the motion-control characteristics of the planar actuator, and suggests incremental improvements for the planar actuator.

## 5. Experimental Motion Control of Long-Stroke Planar Actuator

This chapter presents verification of the 3-DOF drive characteristics of the planar actuator ascertained by experimental study, and describes the experimental results under various conditions.

### 5.1. 3-DOF Motion Control

In order to verify the decoupled 3-DOF motion controls of the planar actuator with superimposed magnetic circuits, drive tests of a mover with 3 DOF were performed.

#### 5.1.1. Experimental Conditions

As mentioned in Section 1.4 and Section 2.5, conventional planar actuators that have been developed to date have spatially separated magnetic circuits for the  $x$ - and  $y$ -directional drives. Therefore, large displacements in the  $x$ -,  $y$ - or  $\alpha$ -directions can separate each pair of armature assemblies from the permanent-magnet array and consequently drastically decrease the driving forces. Therefore, in conventional planar actuators, it is extremely difficult to drive the mover over large displacements on a plane.

I propose a planar actuator that can drive the mover over large displacements in the  $x$ -,  $y$ - and  $\alpha$ -directions using only a few armature conductors. In order to verify the long-stroke motion-control characteristics with 3 DOF, drive tests were performed under the following four conditions:

- (I) Step response for the  $x$ -,  $y$ - and  $\alpha$ -directions:  
Verification of decoupled motion controls in the  $x$ -,  $y$ - and  $\alpha$ -directions, and an evaluation of constant-value controls are performed.
- (II) Sine response for the  $x$ - (or  $y$ -) direction:  
Verification of no interference to the  $y$ - (or  $x$ -) and  $\alpha$ -motions with follow-up controls in the  $x$ - (or  $y$ -) direction is performed.

(III) Sine response for the  $\alpha$ -direction;

Verification of no interference to the  $x$ - and  $y$ -motions with follow-up controls in the  $\alpha$ -direction is performed. Then, in a comparison with the experimental result in (II), the difference between the translational and yaw motion controls is discussed.

(IV) Simultaneous sine response for the  $x$ -,  $y$ - and  $\alpha$ -directions;

Verification of decoupled motion controls in the  $x$ -,  $y$ - and  $\alpha$ -directions, and an evaluation of follow-up controls are performed.

Laser-displacement sensors, as used in this study, cannot detect displacements outside  $\pm 15$  mm from the reference distance, and so in this study position references are given as follows:

- position references in the  $x$ - and  $y$ -directions are in the range within  $\pm 10$  mm.
- position references in the  $\alpha$ -direction are in the range between 5 deg and 15 deg.

The magnitude of mover displacements in the  $x$ - and  $y$ -directions is more than twice the pitch length of the planar actuator  $\tau = 5.3$  mm, and is wide enough to verify the long-stroke motion controls.

### 5.1.2. Experimental Results

Drive tests under the previously mentioned conditions (I)–(IV) in Subsection 5.1.1 were performed. The experimental results are shown as follows under each of the above conditions:

(I) Step response for the  $x$ -,  $y$ - and  $\alpha$ -directions:

Figure 5.1.2-1 shows the experimental results of the mover motions and armature currents when step signals are given as the  $x$ -,  $y$ -, and  $\alpha$ -position references. Figure 5.1.2-1 shows that the mover can be simultaneously driven over large displacements in the  $x$ -,  $y$ -, and  $\alpha$ -directions. There are slight steady-state errors, which are less than 0.3 mm in the  $x$ - and

$y$ -directions, and 0.4 deg in the  $\alpha$ -direction. For instance, during time  $t = 2.5$  s to 3 s, the negative  $q$ -axis  $I_{qx} (< 0)$  can be presumed to always generate negative translational forces  $F_x (< 0)$ , whereas the mover is stationary in this period. Therefore, the friction forces between the mover and ball bearings are presumed to cause this steady-state error. The magnitudes of the steady-state errors are often irregular for time because of the inhomogeneous distribution of the ball bearings. Supplying large armature currents can generate strong driving forces to overcome friction forces. In fact, the armature currents are limited by the  $\pm 3$ -A current capacity of the power amplifiers, thus a reduction in friction forces is an extremely important issue.

(II) Sine response for the  $x$ - (or  $y$ -) direction:

Figure 5.1.2-2 shows the experimental results of the mover motions and armature currents when sine signals are given as the  $x$ -position reference, and references in the  $y$ - and  $\alpha$ -positions are always zero. Figure 5.1.2-2 indicates that the mover can track the sine-reference position, which has a 10-mm amplitude and a 2-s period in the  $x$ -direction, with less interfered motions in the  $y$ - and  $\alpha$ -directions. Figure 5.1.2-3 shows experimental results when sine signals are given as the  $y$ -position reference, and references in the  $x$ - and  $\alpha$ -positions are always zero. Figure 5.1.2-3 indicates that the mover can also track the sine-reference position in the  $y$ -direction with less interfered motions in the  $x$ - and  $\alpha$ -directions.

(III) Sine response for the  $\alpha$ -direction:

Figure 5.1.2-4 shows the experimental results of the mover motions and armature currents when a sine signal is given as the  $\alpha$ -position reference, and references in the  $x$ - and  $y$ -positions are always zero. Figure 5.1.2-4 indicates that the mover can track the sine-reference position, which has a 5-deg amplitude and a 2-s period in the  $\alpha$ -direction, with less interfered motions in the  $x$ - and  $y$ -directions. The position errors shown in Fig. 5.1.2-4 are slightly larger than those in Figs. 5.1.2-2 and 5.1.2-3 and include more error components with 2-s periodicity. That is, there is slightly coupling among the  $x$ -,  $y$ -, and  $\alpha$ -motions. Alignment errors of the laser-displacement sensors and identification errors of the system constants  $K_F$ ,  $K_T$  are presumed to cause the slightly coupled motions. In particular, the  $\alpha$ -

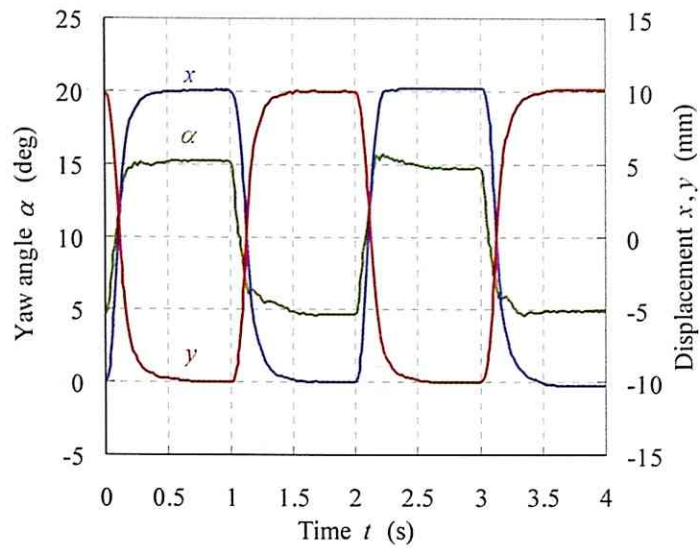
displacements can vary the system constants, and tend to cause identification errors.

(IV) Simultaneous sine response for the  $x$ -,  $y$ - and  $\alpha$ -directions;

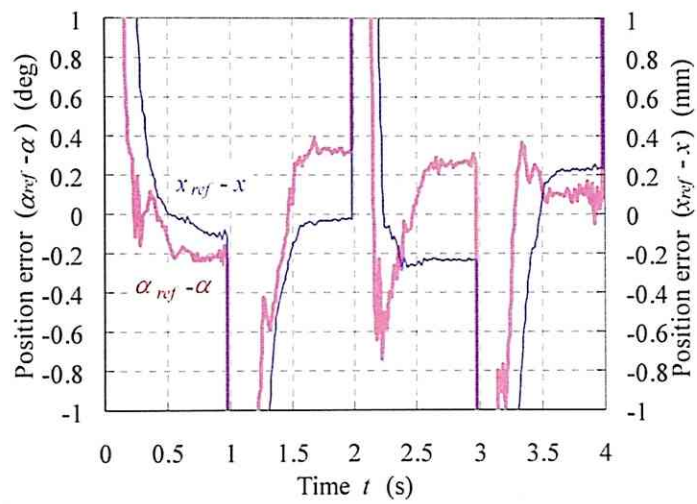
Figure 5.1.2-5 shows the experimental results of the mover motions and armature currents when sine signals are simultaneously given as the  $x$ -,  $y$ -, and  $\alpha$ -position references. Figure 5.1.2-5 indicates that the mover can simultaneously track the three sine-reference positions over a wide movable area. The position errors shown in Fig. 5.1.2-5 are larger than those in Figs. 5.1.2-2, 5.1.2-3, and 5.1.2-4 because the large  $x$ -,  $y$ -, and  $\alpha$ - motions, which are slightly coupled with one another, are simultaneously generated.

Figure 5.1.2-6 shows frequency spectra of the  $x$ -position errors and  $q$ -axis currents for the  $x$ -directional drive in Experiments (II) and (IV), which were calculated from a fast Fourier transform. Each spectrum has a main peak at 0.5 Hz, corresponding to the frequency of the position-reference signals. In Experiment (II), the system constant  $K_{Fx}$  hardly varies because there is less movement in the  $\alpha$ -direction, and therefore the spectrum forms of the  $x$ -position error and  $q$ -axis current in Fig. 5.1.2-6 (a) are similar. In Experiment (IV), the system constant  $K_{Fx}$  varies in a range between 0.074 and 0.028 N/A because the mover travels between 5 deg and 15 deg in the  $\alpha$ -direction as shown in Fig. 5.1.2-5. Thus, the spectrum forms of the  $x$ -position error and  $q$ -axis current in Fig. 5.1.2-6 (b) are slightly different in the lower-frequency region. The ratio of the second harmonic to the fundamental harmonic (0.5 Hz) of the  $q$ -axis current becomes a little larger than that of the  $x$ -position error because of the  $\alpha$ -dependent system constant  $K_{Fx}$ . Therefore, the  $\alpha$ -directional fluctuation is presumed to have a slight influence on the  $x$ - and  $y$ -motions.

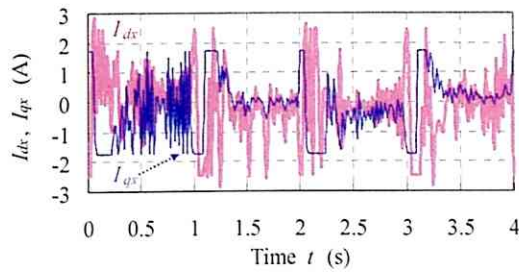
From these experiments, I successfully demonstrated that the mover could travel over large displacements in the  $x$ -,  $y$ -, and  $\alpha$ -directions simultaneously by controlling only two polyphase armature currents. Furthermore, the mover can travel—especially in the  $x$ - and  $y$ -directions—over an infinitely wide area, in principle, by lengthening all the armature conductors. In order to further improve drive performance, reducing the friction forces between the mover and bearings, and weakening the coupling of the mover motions in the  $x$ -,  $y$ -, and  $\alpha$ -directions are extremely important.



(a) Mover position in the  $x$ -,  $y$ - and  $\alpha$ -directions.

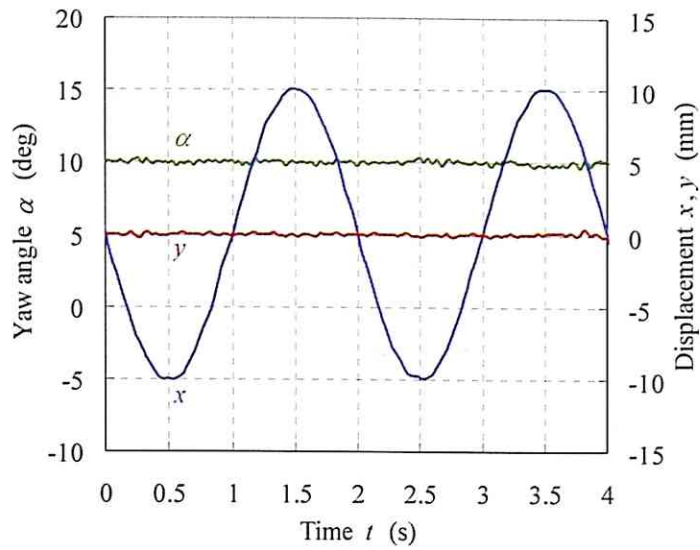


(b) Position errors in the  $x$ -,  $y$ - and  $\alpha$ -directions.

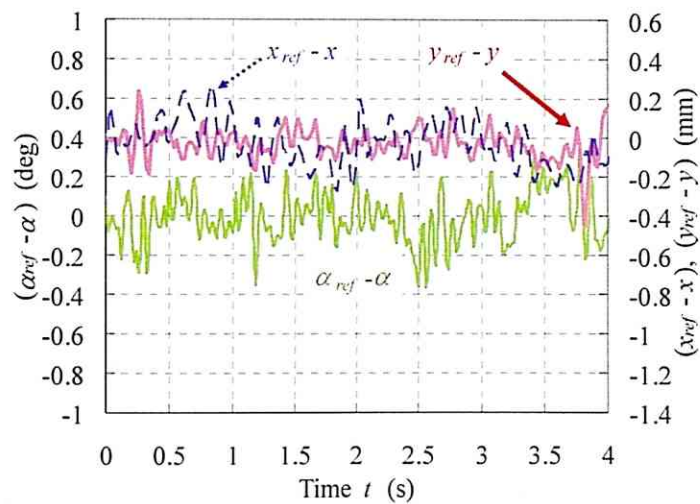


(c) Armature currents for  $x$ -directional drive in the  $dq$ -frame.

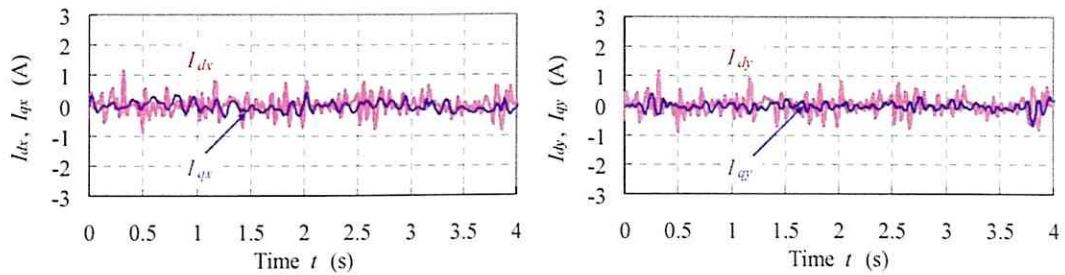
Fig. 5.1.2-1: Experimental results of step response for  $x$ -,  $y$ - and  $\alpha$ -directions.



(a) Mover position in the  $x$ -,  $y$ - and  $\alpha$ -directions.

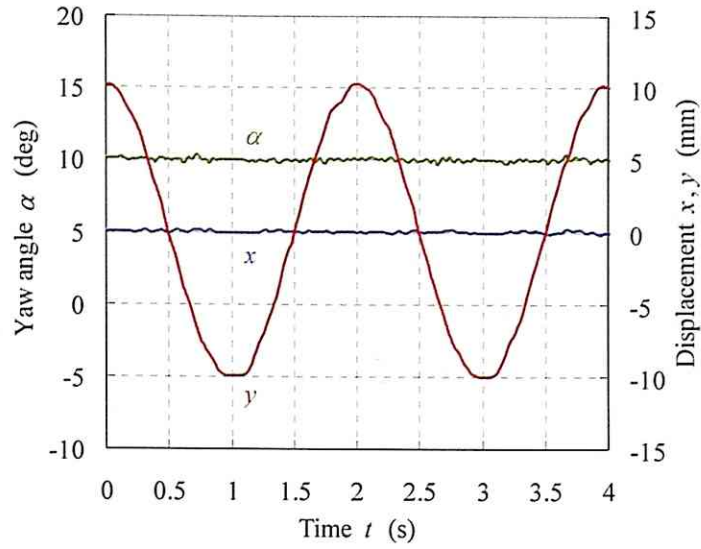


(b) Position errors in the  $x$ -,  $y$ - and  $\alpha$ -directions.

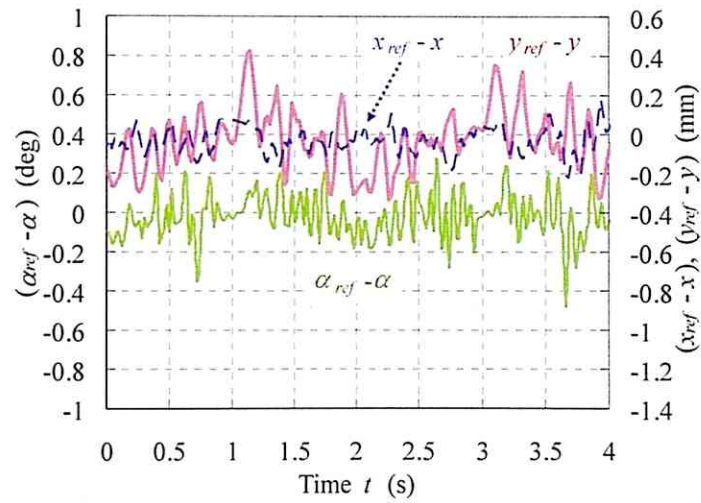


(c) Armature currents for the  $x$ - and  $y$ -directional drive in the  $dq$ -frame.

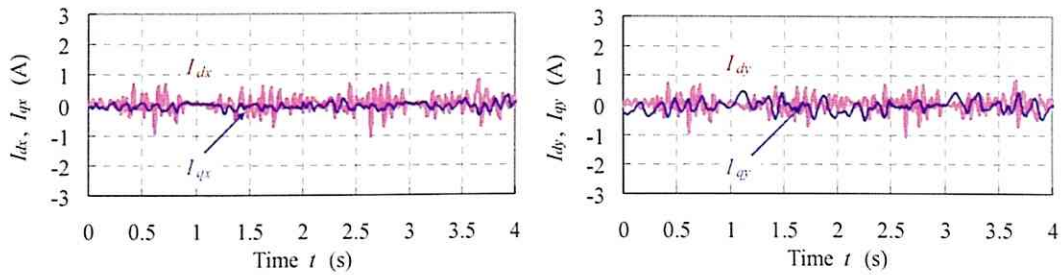
Fig. 5.1.2-2: Experimental results of sine response for  $x$ -direction.



(a) Mover position in the  $x$ -,  $y$ - and  $\alpha$ -directions.

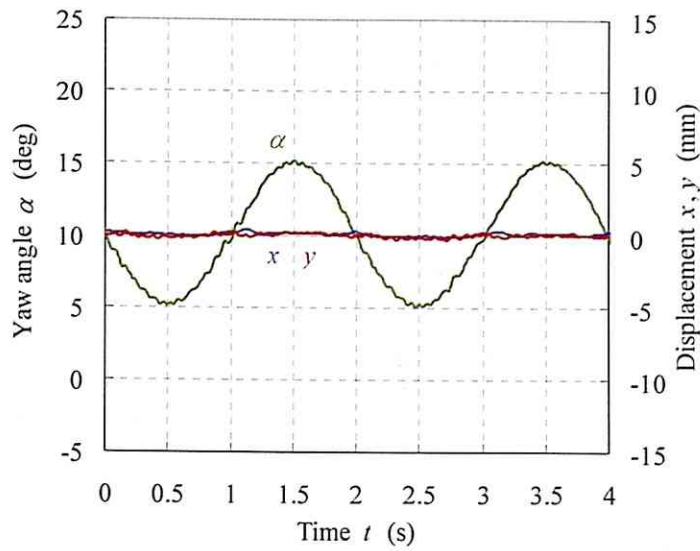


(b) Position errors in the  $x$ -,  $y$ - and  $\alpha$ -directions.

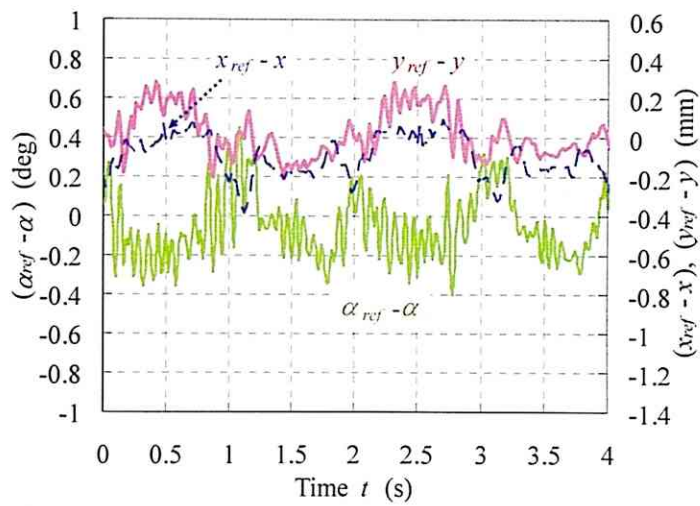


(c) Armature currents for the  $x$ - and  $y$ -directional drive in the  $dq$ -frame.

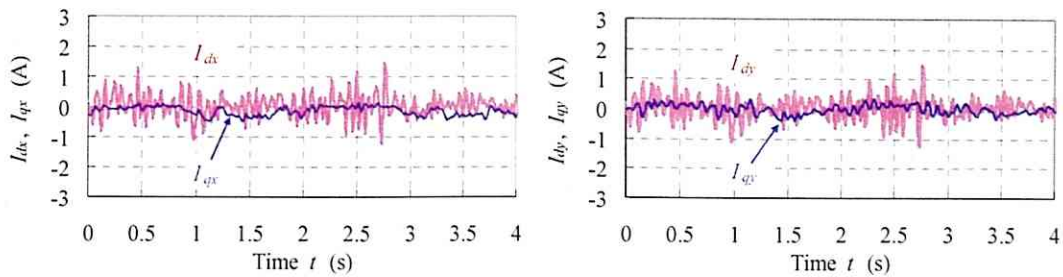
Fig. 5.1.2-3: Experimental results of sine response for  $y$ -direction.



(a) Mover position in the  $x$ -,  $y$ - and  $\alpha$ -directions.

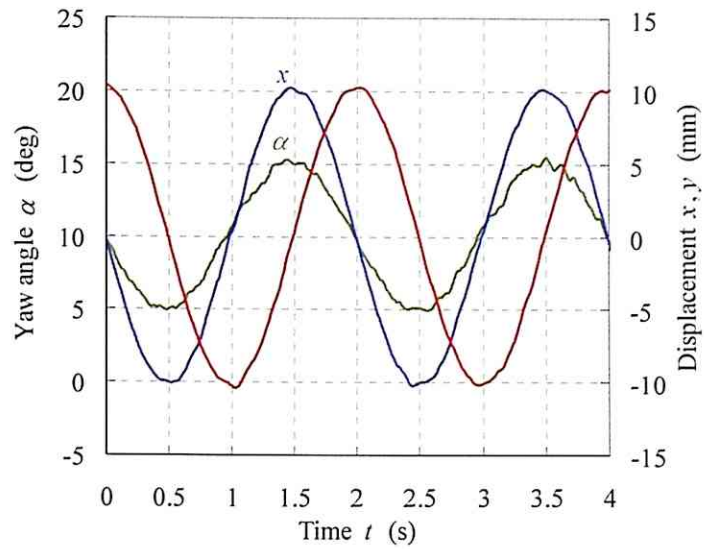


(b) Position errors in the  $x$ -,  $y$ - and  $\alpha$ -directions.

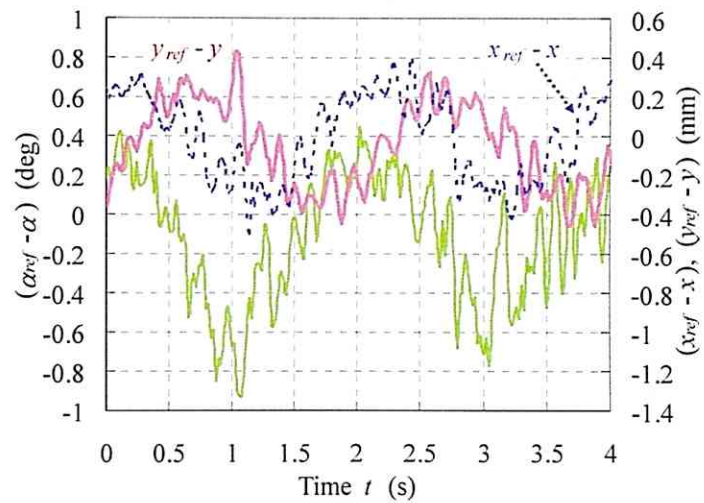


(c) Armature currents for the  $x$ - and  $y$ -directional drive in the  $dq$ -frame.

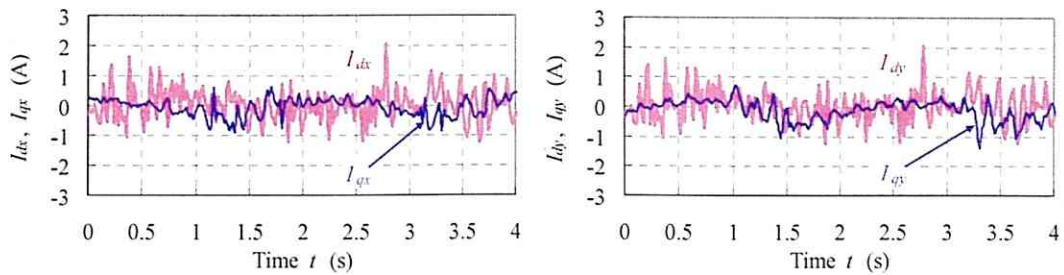
Fig. 5.1.2-4: Experimental results of sine response for  $\alpha$ -direction.



(a) Mover position in the  $x$ -,  $y$ - and  $\alpha$ -directions.

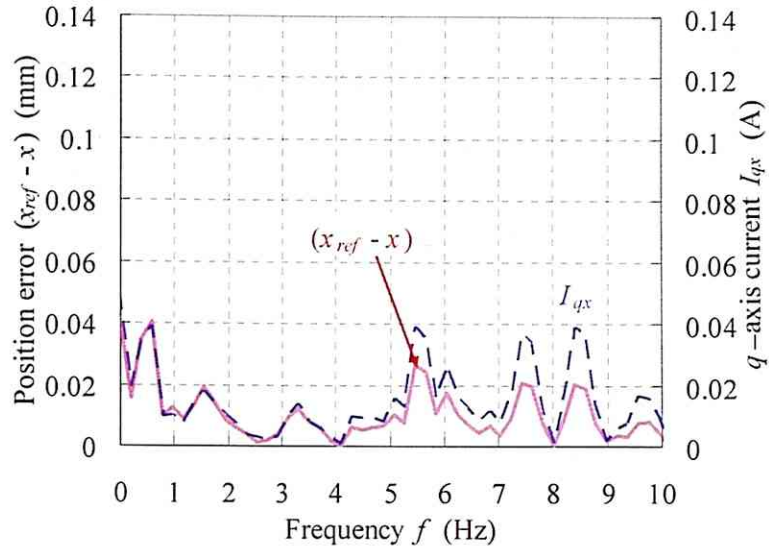


(b) Position errors in the  $x$ -,  $y$ - and  $\alpha$ -directions.

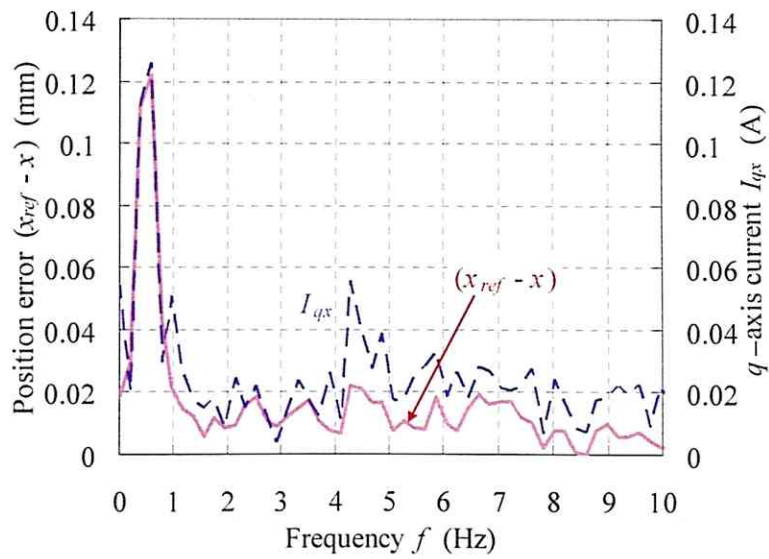


(c) Armature currents for the  $x$ - and  $y$ -directional drive in the  $dq$ -frame.

Fig. 5.1.2-5: Experimental results of simultaneous sine response for  $x$ -,  $y$ - and  $\alpha$ -directions.



(a) Frequency spectra in Experiment (II).



(b) Frequency spectra in Experiment (IV).

Fig. 5.1.2-6: Frequency spectra of  $x$ -position errors  $(x_{ref} - x)$  and  $q$ -axis currents  $I_{qx}$  for  $x$ -directional drive in Experiments (II) and (IV).

## 5.2. Long-Stroke Yaw Motion Control

In my proposed planar actuator, even if a large  $\alpha$ -displacement of the mover occurs, the driving forces decrease less than conventional planar actuators because the magnetic circuits for the  $x$ -,  $y$ -, and  $\alpha$ -directional drives are always formed. The planar actuator has a mover capable of infinitely-large translational motions on a plane, in principle, as mentioned in Section 5.1. This section presents experimental verification of the movable area in the  $\alpha$ -direction.

### 5.2.1. Experimental Conditions

The planar actuator can theoretically generate the driving forces in the range within the yaw angle  $\alpha = \pm 30$  deg as shown in Fig. 3.3.2-3. With this in mind, in order to verify the movable area in the  $\alpha$ -direction, the following drive tests were performed:

- (V)  $\alpha$ -directional drive at the yaw angle  $\alpha \approx 0$  deg:

Whereas the translational forces in the  $x$ - and  $y$ -directions are maximum at the yaw angle  $\alpha = 0$  deg, torque in the  $\alpha$ -direction cannot be generated. Therefore, controllability of the  $\alpha$ -motion is presumed to deteriorate at the yaw angle  $\alpha \approx 0$  deg. Then, in order to verify the motion-control characteristics at the yaw angle  $\alpha \approx 0$  deg, ramp response for the  $\alpha$ -direction was investigated in the same range.

- (VI)  $\alpha$ -directional drive at the yaw angle  $\alpha > 20$  deg:

Increasing the yaw angle  $\alpha$  can decrease the driving forces especially at the yaw angle  $\alpha > 20$  deg. Then, in order to verify the movable area and motion-control characteristics at the yaw angle  $\alpha > 20$  deg, ramp response for the  $\alpha$ -direction was investigated in the same range.

- (VII) 90-deg step response for the  $\alpha$ -direction:

The driving forces of the planar actuator have a 90-deg periodicity for the  $\alpha$ -direction because of the symmetric magnetized mover. Furthermore, the driving forces are generated in the range within the yaw angle  $\alpha = \pm 30$  deg in the 90-deg periodicity. Then, in order to verify feasibility of periodic 90-deg stepping drives in the  $\alpha$ -direction, a 90-deg step response was investigated.

As mentioned in Section 4.2, the position-sensing system, consisting of three laser-displacement sensors, can theoretically detect the mover positions in the range within  $\alpha_{\min} = -19 \text{ deg} < \text{the yaw angle } \alpha < \alpha_{\max} = 31 \text{ deg}$ . The mover position can be detected every 90-deg for the  $\alpha$ -direction because of the square structure of the mover, and, so the measurable area for the  $\alpha$ -direction can be expressed as shown in Fig. 5.2.1-1. In Experiment (VII), however, the mover is assumed to travel over the unmeasurable area, which is in the range outside  $\alpha_{\min} < \alpha < \alpha_{\max}$ . Then, in Experiment (VII), when generating sufficient driving forces and measuring the mover positions are capable as shown by dashed lines in Fig. 5.2.1-1, the control currents are supplied to the armature conductors.

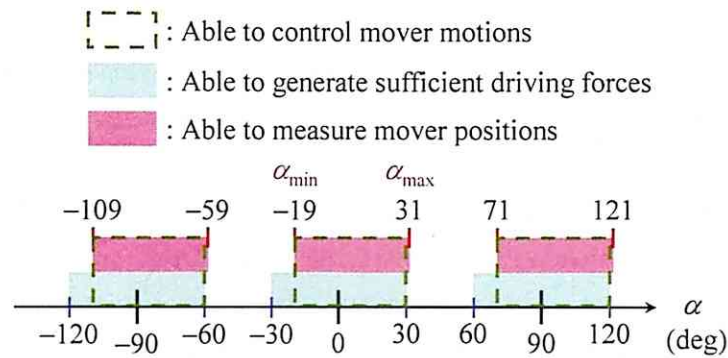


Fig. 5.2.1-1: Characteristics of planar actuator for  $\alpha$ -direction.

## 5.2.2. Experimental Results

Drive tests under the previously mentioned conditions (V)–(VII) in Subsection 5.2.1 were performed. The experimental results are shown as follows under each of the above conditions:

- (V)  $\alpha$ -directional drive at the yaw angle  $\alpha \approx 0 \text{ deg}$ :

Figure 5.2.2-1 shows the experimental results of the mover motions and armature currents for ramp response with the position references  $(x_{ref}, y_{ref}) = (0, 0)$  and  $\alpha_{ref} = -5 + t \text{ (deg)}$ , where  $t$  is time. Figure 5.2.2-1 indicates that the mover can travel in the  $\alpha$ -direction with 0.2-mm accuracy in the  $x$ - and  $y$ -directions in the range within the yaw angle  $\alpha = \pm 5 \text{ deg}$ . When the yaw angle  $\alpha$  closes to 0 deg, the large  $d$ -axis currents  $I_{dx}$  and  $I_{dy}$  are required to

control the  $\alpha$ -position. In the range within the yaw angle  $\alpha = \pm 1$  deg, not only the  $\alpha$ -position, but also the  $x$ - and  $y$ -positions become more oscillatory. The current capacity of the power amplifiers is presumed to be the reason the  $d$ -axis currents are insufficient to control the  $\alpha$ -motion, and consequently cause the oscillation in the  $\alpha$ -position. Due to the slightly asymmetric magnetization of the manufactured permanent-magnet mover, the  $d$ -axis currents  $I_{dx}$  and  $I_{dy}$  generate the translational forces  $F_x$  and  $F_y$  slightly coupled with the torques  $T_z$ , respectively. At the yaw angle  $\alpha \approx 0$  deg, in particular, influence from the coupled translational forces is presumed to emerge because the  $d$ -axis currents  $I_{dx}$  and  $I_{dy}$  are large.

(VI)  $\alpha$ -directional drive at the yaw angle  $\alpha > 20$  deg:

Figure 5.2.2-2 shows the experimental results of the mover motions and armature currents for ramp response with the position references  $(x_{ref}, y_{ref}) = (0, 0)$  and  $\alpha_{ref} = 18 + t$  (deg). Figure 5.2.2-2 indicates that the mover can travel in the  $\alpha$ -direction with 0.4-deg accuracy in the  $\alpha$ -direction at the yaw angle  $\alpha < 26$  deg. When the yaw angle  $\alpha$  becomes larger, the large  $q$ -axis currents  $I_{qx}$  and  $I_{qy}$  are required to control the  $x$ - and  $y$ -positions. At the yaw angle  $\alpha > 22$  deg (time  $t > 4$  s), the  $q$ -axis currents  $I_{qx}$  and  $I_{qy}$  are limited by the maximum current = 1.7 A. The  $\alpha$ -motion obtained in Experiment (V) is more oscillatory than that in Experiment (VI). The  $q$ -axis currents  $I_{qx}$  and  $I_{qy}$  can generate the torques  $T_z$  slightly coupled with the translational forces  $F_x$  and  $F_y$ , respectively. Influence by the coupled torques is presumed to emerge because the  $q$ -axis currents  $I_{qx}$  and  $I_{qy}$  in Experiment (VI) are larger. At the yaw angle  $\alpha > 26$  deg (time  $t > 8$  s), the mover is stationary, and, therefore the driving forces required to overcome the friction forces between the mover and ball bearings cannot be generated.

(VII) 90-deg step response for the  $\alpha$ -direction:

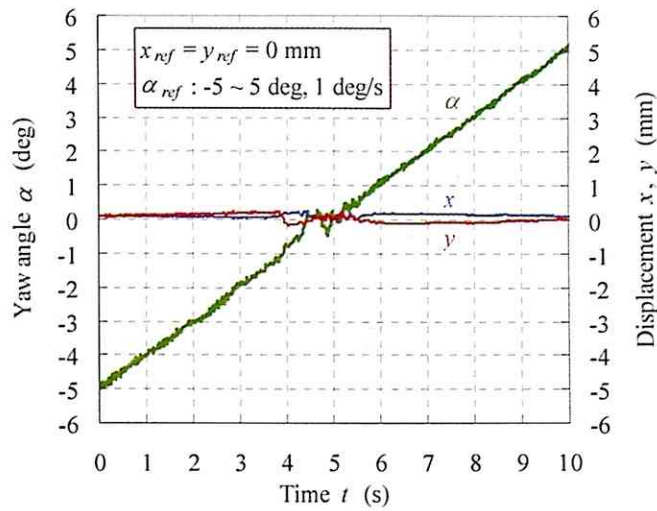
Figure 5.2.2-3 shows experimental results of the mover motions and armature currents for 90-deg step response with the initial positions  $(x_{in}, y_{in}, \alpha_{in}) = (0, 0, 10)$  and the position references  $(x_{ref}, y_{ref}, \alpha_{ref}) = (0, 0, 100)$ . Figure 5.2.2-3 indicates that a 90-deg stepping drive can be realized with 0.1-deg accuracy and 0.4-s settling time. The sensor outputs  $S_1$ ,  $S_2$ , and  $S_3$  are minimum at time  $t = 0.18$  s, 0.11 s, and 0.10 s, and at the same time, irradiated surfaces by Sensor 1, Sensor 2, and Sensor 3 are switched,

respectively. At time  $t = 0.28$  s, summation of the sensor outputs ( $S_2 + S_3$ ) is maximum. Therefore, the mover positions cannot be detected in the range within  $0.10 \text{ s} < \text{time } t < 0.28 \text{ s}$ , and in the experiment the armature currents were not supplied in this range. The yaw angle  $\alpha_{\min}$  is experimentally obtained to be  $-14$  deg, which is not in complete agreement with the  $-19$  deg theoretically obtained. The disagreement is presumed to be caused by alignment errors of the laser-displacement sensors.

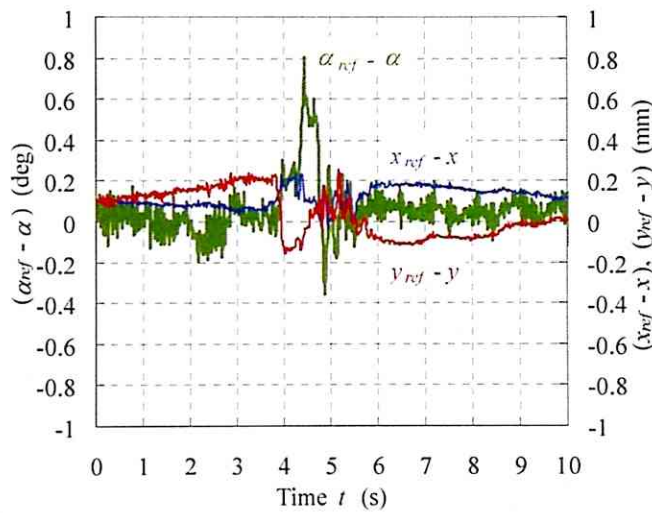
The planar actuator generates the same driving forces every 90-deg in the  $\alpha$ -direction because of the symmetric magnetized mover. So, at the yaw angle  $\alpha > (\alpha_{\min} + 90)$  deg, corresponding to time  $t > 0.28$  s, the mover motions can be controlled. At time  $t < 0.4$  s, there are the position errors ( $x_{ref} - x$ ) and ( $y_{ref} - y$ ) in the  $x$ - and  $y$ -directions. The  $d$ -axis currents  $I_{dx}$  and  $I_{dy}$  can generate the translational forces  $F_x$  and  $F_y$  slightly coupled with the torques  $T_z$ , and influence of the coupled torques is presumed to emerge because of the large  $d$ -axis currents  $I_{dx}$  and  $I_{dy}$ .

Figure 5.2.2-4 shows experimental results of the mover motions and armature currents for multiple 90-deg step responses with the position references  $(x_{ref}, y_{ref}) = (0, 0)$ ,  $\alpha_{ref} = 100, 190, 280, \text{ or } 370$  deg, and the initial positions  $(x_{in}, y_{in}, \alpha_{in}) = (0, 0, 10)$ . In each 90-deg stepping drive, similar drive characteristics were obtained, and—especially—similar position errors in the  $x$ - and  $y$ -directions were generated due to the slightly coupled translational forces.

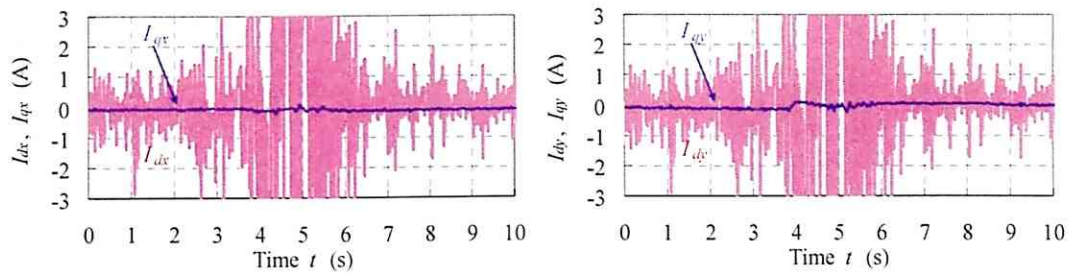
From these experiments, I successfully demonstrated that the mover could travel in the  $\alpha$ -direction over the widest movable area, which is in the range within the yaw angle  $\alpha = \pm 26$  deg, and perform 90-deg stepping drives by controlling two polyphase currents, which is lowest number of phases for the armature currents. Reducing the friction forces and weakening the slightly coupled 3-DOF forces are required to further improve drive performance.



(a) Mover position in the  $x$ -,  $y$ - and  $\alpha$ -directions.

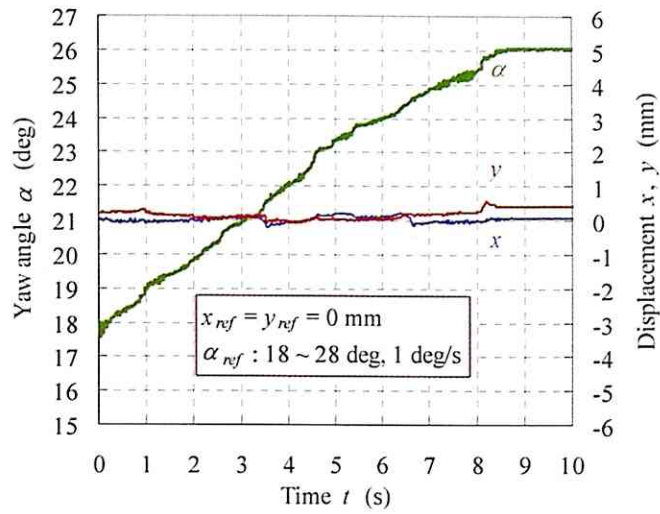


(b) Position errors in the  $x$ -,  $y$ - and  $\alpha$ -directions.

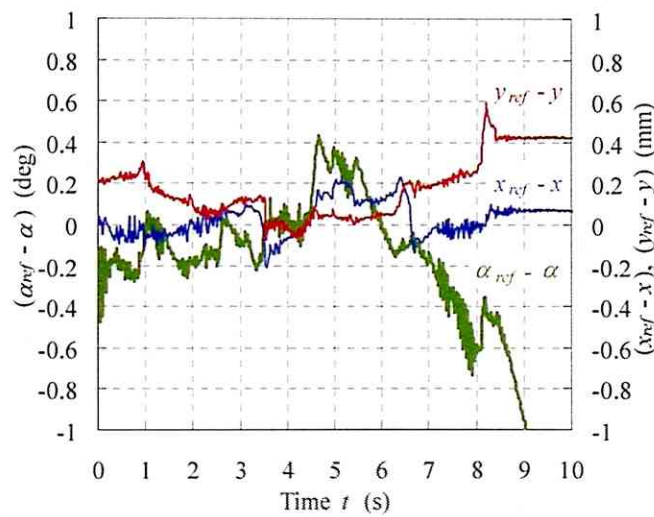


(c) Armature currents for the  $x$ - and  $y$ -directional drives in the  $dq$ -frame.

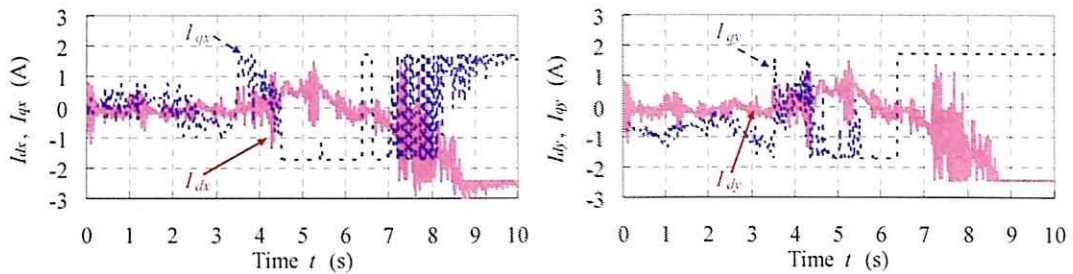
Fig. 5.2.2-1: Experimental results of ramp response for  $\alpha$ -direction at yaw angle  $\alpha \approx 0$  deg.



(a) Mover position in the  $x$ -,  $y$ - and  $\alpha$ -directions.

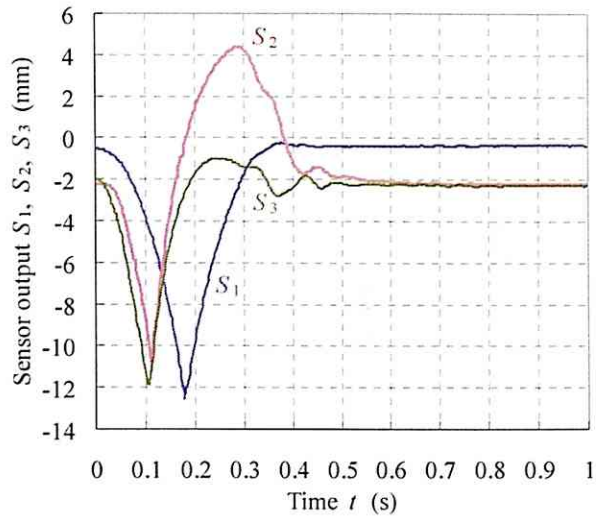


(b) Position errors in the  $x$ -,  $y$ - and  $\alpha$ -directions.

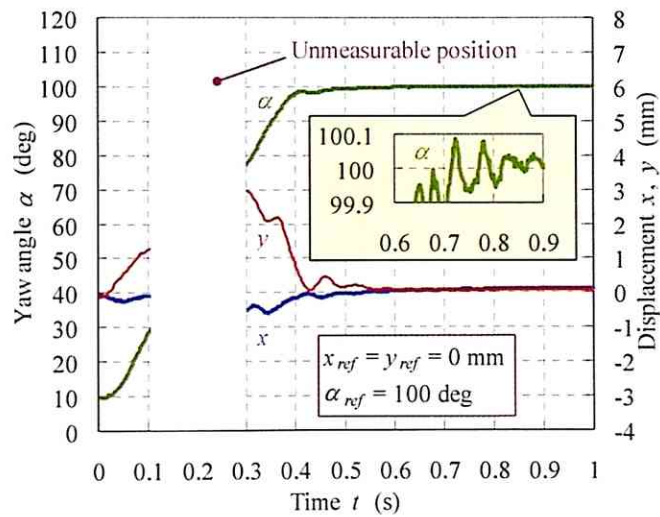


(c) Armature currents for the  $x$ - and  $y$ -directional drives in the  $dq$ -frame.

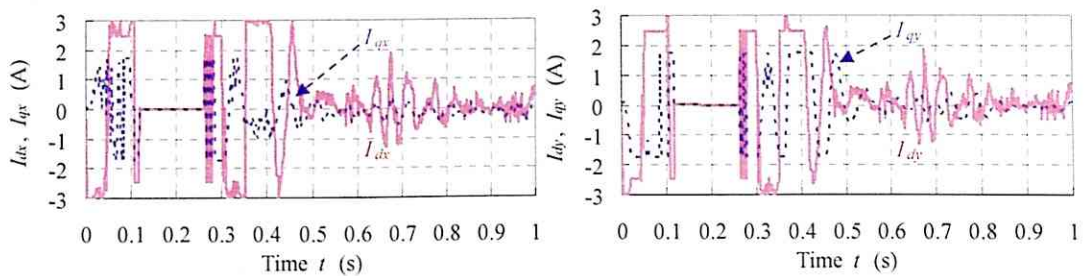
Fig. 5.2.2-2: Experimental results of ramp response for  $\alpha$ -direction at yaw angle  $\alpha > 20$  deg.



(b) Mover position in the  $x$ -,  $y$ - and  $\alpha$ -directions.

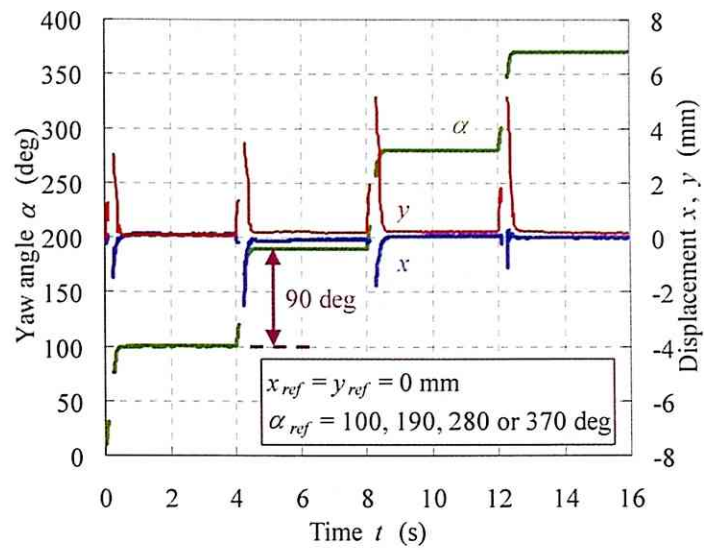


(b) Mover position in the  $x$ -,  $y$ - and  $\alpha$ -directions.

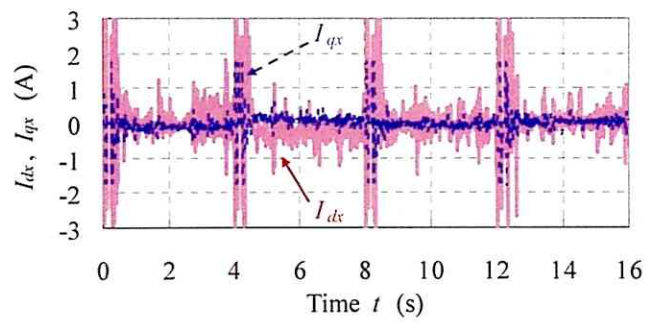


(c) Armature currents for the  $x$ - and  $y$ -directional drives in the  $dq$ -frame.

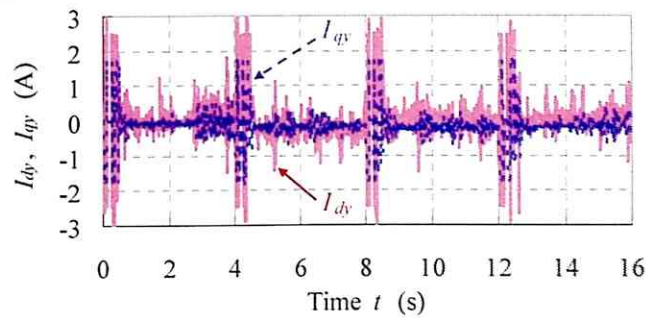
Fig. 5.2.2-3: Experimental results of 90-deg stepping response for  $\alpha$ - direction.



(a) Mover position in the  $x$ -,  $y$ - and  $\alpha$ -directions.



(b) Armature currents for the  $x$ -directional drive in the  $dq$ -frame.



(c) Armature currents for the  $y$ -directional drive in the  $dq$ -frame.

Fig. 5.2.2-4: Experimental results of multiple 90-deg stepping response for  $\alpha$ -direction.

### 5.3. Issues toward Incremental Improvements

From the experimental results in Section 5.1 and Section 5.2, I demonstrate that the planar actuator has sophisticated drive performances as follows:

- capable of decoupled 3-DOF motion controls on a plane.
- only two polyphase currents (six currents).
- extendible  $x$ - and  $y$ -movable area regardless of the number of armature conductors.
- wide  $\pm 26$  deg  $\alpha$ -movable area.

Looking ahead, I would like to clarify some technical issues toward incremental improvements: first, reducing the steady-state errors caused by the friction forces between the mover and ball bearings, and second, weakening the slightly coupled motions caused by the alignment error of the sensors and the identification error of the system constants.

#### 5.3.1. Eliminating Friction Forces

Ball bearings were easily installed in the experimental system as the suspension mechanism for the mover, and can guide the mover on a plane with relatively small friction forces. However, these friction forces often cause problems in realizing high-performance motion controls. Therefore, contactless suspension of the mover is preferable. As mentioned in Subsection 1.2.4, there are two contactless suspension methods: one is air bearings, and the other is magnetic bearings. Air bearings can suspend heavy loads, however, as they require compressors, pneumatic lines, and precompression mechanisms. Therefore, air bearings are structurally larger, and are not suitable for the small planar actuator in this study. Magnetic bearings, on the other hand, are better suited for the armature conductor and magnet mover, if a magnetic suspension system is designed so as to generate stable suspension forces with 3-DOF motions on a controlled plane.

### 5.3.2. Calibrating Position Sensing

Alignment errors with the laser-displacement sensors and output-signal deviation caused by the experimental environment resulted in errors in measuring the mover positions. To compensate for the measurement errors, calibration of the position sensing system is a vital requirement. Although calibration of position-sensing systems with MDOF has not been reported to date, error mapping and additional sensors for calibration are presumed to be required.

## 5.4. Summary of Chapter 5

This chapter describes the experimental results of long-stroke 3-DOF motion controls to verify the fundamental drive characteristics of the planar actuator. From these results, I successfully demonstrated that the 3-DOF motions of the mover can be independently controlled by two polyphase armature currents. The movable area in the  $x$ - and  $y$ -directions is infinitely wide, and that in the  $\alpha$ -direction is in the range within  $\pm 26$  deg, meaning the planar actuator has the widest movable area of all planar actuators that have only two polyphase armature conductors. Then, in order to improve the performance, for instance, response and precision, contactless suspension of the mover and calibration of the position sensing system are necessary.